Inhibition of the renal apical sodium dependent bile acid transporter prevents cholemic nephropathy in mice with obstructive cholestasis

Ahmed Ghallab[1,2,*], Daniela González[1], Ellen Strängberg[3], Ute Hofmann[4], Maiju Myllys[1], Reham Hassan[1,2], Zaynab Hobloss[1], Lisa Brackhagen[1], Brigitte Begher-Tibbe[1], Julia C. Duda[5], Carolin Drenda[5], Franziska Kappenberg[5], Joerg Reinders[1], Adrian Friebel[6], Mihael Vucur[7], Monika Turajski[1], Abdel-latief Seddek[2], Tahany Abbas[8], Noha Abdelmageed[9], Samy A.F. Morad[10], Walaa Morad[8], Amira Hamdy[2], Wiebke Albrecht[1], Naim Kittana[11], Mohyeddin Assali[12], Nachiket Vartak[1], Christoph van Thriel[1], Ansam Sous[12], Patrick Nell[1], Maria Villar-Fernandez[1], Cristina Cadenas[1], Erhan Genc[13], Rosemarie Marchan[1], Tom Luedde[7], Peter Åkerblad[3], Jan Mattsson[3], Hanns-Ulrich Marschall[14,+], Stefan Hoehme[6], Guido Stirnimann[15], Matthias Schwab[4,16,17], Peter Boor[18], Kerstin Amann[19], Jessica Schmitz[20], Jan H. Bräsen[20], Jörg Rahnenführer[5], Karolina Edlund[1], Saul J. Karpen[21], Benedikt Simbrunner[22,23], Thomas Reiberger[22,23], Mattias Mandorfer[22,23], Michael Trauner[22,24], Paul A. Dawson[21,#], Erik Lindström[3,#], Jan G. Hengstler[1,*,#]

Check for updates

See Editorial, pages 188–190

Background & Aims: Cholemic nephropathy (CN) is a severe complication of cholestatic liver diseases for which there is no specific treatment. We revisited its pathophysiology with the aim of identifying novel therapeutic strategies.
Methods: Cholestasis was induced by bile duct ligation (BDL) in mice. Bile flux in kidneys and livers was visualized by intravital imaging, supported by MALDI mass spectrometry imaging and liquid chromatography-tandem mass spectrometry. The effect of AS0369, a systemically bioavailable apical sodium-dependent bile acid transporter (ASBT) inhibitor, was evaluated by intravital imaging, RNA-sequencing, histological, blood, and urine analyses. Translational relevance was assessed in kidney biopsies from patients with CN, mice with a humanized bile acid (BA) spectrum, and via analysis of serum BAs and KIM-1 (kidney injury molecule 1) in patients with liver disease and hyperbilirubinemia.
Results: Proximal tubular epithelial cells (TECs) reabsorbed and enriched BAs, leading to oxidative stress and death of proximal TECs, casts in distal tubules and collecting ducts, peritubular capillary leakiness, and glomerular cysts. Renal ASBT inhibition by AS0369 blocked BA uptake into TECs and prevented kidney injury up to 6 weeks after BDL. Similar results were obtained in mice with humanized BA composition. In patients with advanced liver disease, serum BAs were the main determinant of KIM-1 levels. ASBT expression in TECs was preserved in biopsies from patients with CN, further highlighting the translational potential of targeting ASBT to treat CN.
Conclusions: BA enrichment in proximal TECs followed by oxidative stress and cell death is a key early event in CN. Inhibiting renal ASBT and consequently BA enrichment in TECs prevents CN and systemically decreases BA concentrations.

Introduction

Acute kidney injury (AKI) is a frequent complication in patients with liver disease that leads to high morbidity and mortality[1,2] and has several causes, particularly hemodynamic changes, and infections.[1,3] However, an underestimated and increasingly acknowledged[4,5] cause of AKI in liver diseases is cholemic nephropathy (CN),[2,6,7] which describes renal dysfunction together with characteristic renal histological features such as tubular cell injury and Hall's stain-positive bilirubin casts. It has long been known that the risk of AKI is increased in jaundiced patients.[8,9] CN occurs in individuals with liver diseases of different etiologies, including obstructive cholestasis, decompensated cirrhosis/acute-on-chronic liver failure, alcohol-associated hepatitis, and acute liver injury/failure.[2,3] Despite their different etiology, all these disorders are associated with variable degrees of cholestasis. The frequency of CN is likely underestimated in clinical practice since the diagnosis is based on biopsy-proven tubular injury with bilirubin casts. However, kidney biopsies in patients with hepatic dysfunction are often

not performed because of a high risk of bleeding.[6] Postmortem kidney autopsy studies of patients with decompensated cirrhosis and acute-on-chronic liver failure hospitalized because of AKI showed histologically proven CN in 75% and 25% of the samples, respectively.[10]

Despite the association with cholestasis, the underlying pathophysiological mechanisms of CN remain unclear.[3,6] Common bile duct ligation (BDL) in mice caused renal tubular epithelial cell (TEC) injury and histological as well as functional alterations mimicking human CN, suggesting a pathogenic role of bile acids (BAs).[11] Increasing the hydrophilicity of the BA pool either via norursodeoxycholic acid feeding or farnesoid X receptor knockout ameliorated CN.[12] These findings suggest that elevated circulating BA levels lead to increased glomerular filtration, resulting in elevated renal levels of BAs that are cytotoxic to epithelial cells lining the tubules and collecting ducts. Nevertheless, there is an ongoing debate about the causal role of BAs *vs.* other cholephiles that are increased in cholestasis, such as bilirubin or inflammatory mediators, in the development of CN.[2,13,14]

Here, we used intravital imaging[15,16] to directly observe glomerular filtration and tubular BA reabsorption. We report that massively increased reabsorption of BAs into proximal TECs in cholestasis is critical for CN pathogenesis. Systemic inhibition of the BA uptake carrier apical sodium-dependent BA transporter (ASBT) with the novel compound AS0369 blocked BA uptake from the tubular lumen and shows therapeutic potential for the treatment of CN.

Materials and methods

A detailed description of all methods is provided in the supplementary methods and in the supplementary CTAT table.

Renal biopsies of patients with CN and human serum

Renal biopsies from patients with CN (21) and without CN (11) were collected from two cohorts: Hannover cohort (14 CN and 4 non-CN biopsies), and Erlangen cohort (7 CN and 7 non-CN biopsies; Table S1A). Serum samples of patients with acute and/or chronic liver disease (n = 67) and bilirubin >6 mg/dl undergoing HVPG measurement ± transjugular liver biopsy at the Vienna Hepatic Hemodynamic Lab were selected from a prospective registry with a biobank (Table S1B). Healthy individuals (n = 36) were volunteers from Dortmund (Table S1B). The clinical studies were conducted according to the ethical guidelines of the 1975 Helsinki Declaration and its later amendments as approved by the local ethics committees (no. 1262/2017, 4415, 22-150-D). Informed consent was obtained from all participants.

Mice, induction of obstructive cholestasis, and AS0369 administration

Eight-to-10-week-old male and female C57BL/6N (Janvier Labs, France) or *Cyp2c70*^{-/-} and corresponding C57BL/6J wild-type (Dawson, Karpen Lab) mice were used. All experiments were approved by the local animal welfare committee (LANUV, North Rhine-Westphalia, Germany, application number: 81-02.04.2022.A286). To induce biliary obstruction, as a model for severe cholestasis, the extrahepatic common bile duct was ligated as previously described.[16] A stock formulation of the ASBT inhibitor AS0369 was prepared as a suspension, and

doses of 15, 30, 60 and 120 mg/kg b.w. were administered orally by gavage twice daily.

Intravital imaging

Functional intravital imaging of mouse livers and kidneys was performed using a two-photon microscope (Zeiss, Germany) as previously described.[15]

Results

Enhanced uptake of BAs into renal TECs in obstructive cholestasis

To study the mechanisms by which cholestatic liver disease leads to nephropathy, the liver-kidney axis was analyzed time-dependently in mice up to 12 weeks after BDL or sham operation. In agreement with previous studies,[11,12,16] BDL led to excessive accumulation of bile in the gallbladder, transient elevation of plasma transaminases, and to time-dependent elevation of plasma alkaline phosphatase activity (Fig. S1A-C). Histological analysis of the liver showed progressive ductular reaction, leukocyte infiltration, and fibrosis (Fig. S1D). Intravital imaging of the liver after intravenous bolus injection of fluorophore-coupled taurocholic acid (TCA) demonstrated efficient uptake from the sinusoidal blood into hepatocytes within minutes, followed by secretion into the bile canaliculi in control mice. In contrast, TCA remained elevated in the sinusoidal blood of BDL mice during the entire imaging period (Fig. S2; Video S1).

To visualize the transport of BAs in the kidney of mice with obstructive cholestasis, a bolus of the fluorophore-coupled TCA was administered into the tail vein on day 21 after BDL or sham operation, and intravital videos were recorded. In the controls, a transient, very weak increase of TCA-associated fluorescence was quantified in the peritubular capillaries, then in the tubular lumen and the corresponding TEC (Fig. 1A,B; Video S2A). After BDL, the intensity of the TCA signal was higher and remained increased in the peritubular capillaries (Fig. 1A,C; Video S2B). In addition, a strong uptake of TCA via the apical membrane was observed in some TECs, further named type A, while only a minor increase was seen in other TECs, named type B (Fig. 1A, C). Thus, spatio-temporal intravital analysis revealed strongly reduced BA uptake by the liver, consequently higher and persistently increased blood concentrations, enhanced glomerular filtration and enrichment of BAs in TECs after BDL.

To investigate whether these observations could be reproduced without the use of fluorescent markers, a time-resolved comprehensive analysis of endogenous BAs was performed up to 12 weeks after BDL (Fig. 1D). First, TCA, an abundant endogenous BA in mice, was analyzed in liver and kidney tissues by matrix-assisted laser desorption ionization-mass spectrometry imaging (MALDI-MSI). In liver tissue, BDL caused a transient TCA increase on day 1, which decreased thereafter, but remained above control values (Figs 1E,F and S3). In contrast, in the kidneys, a progressive time-dependent increase in endogenous TCA was detected after BDL (Figs 1E,F and Fig. S3). The results of MALDI-MSI were confirmed by liquid chromatography-tandem mass spectrometry analysis of endogenous BAs in tissue homogenate (Fig. 1G). Blood concentrations of BAs were massively increased at all time intervals after BDL (Fig. 1G). Altogether, these data confirm the adaptive response of the liver to cholestatic conditions and suggest an impaired ability of the kidney to adapt.
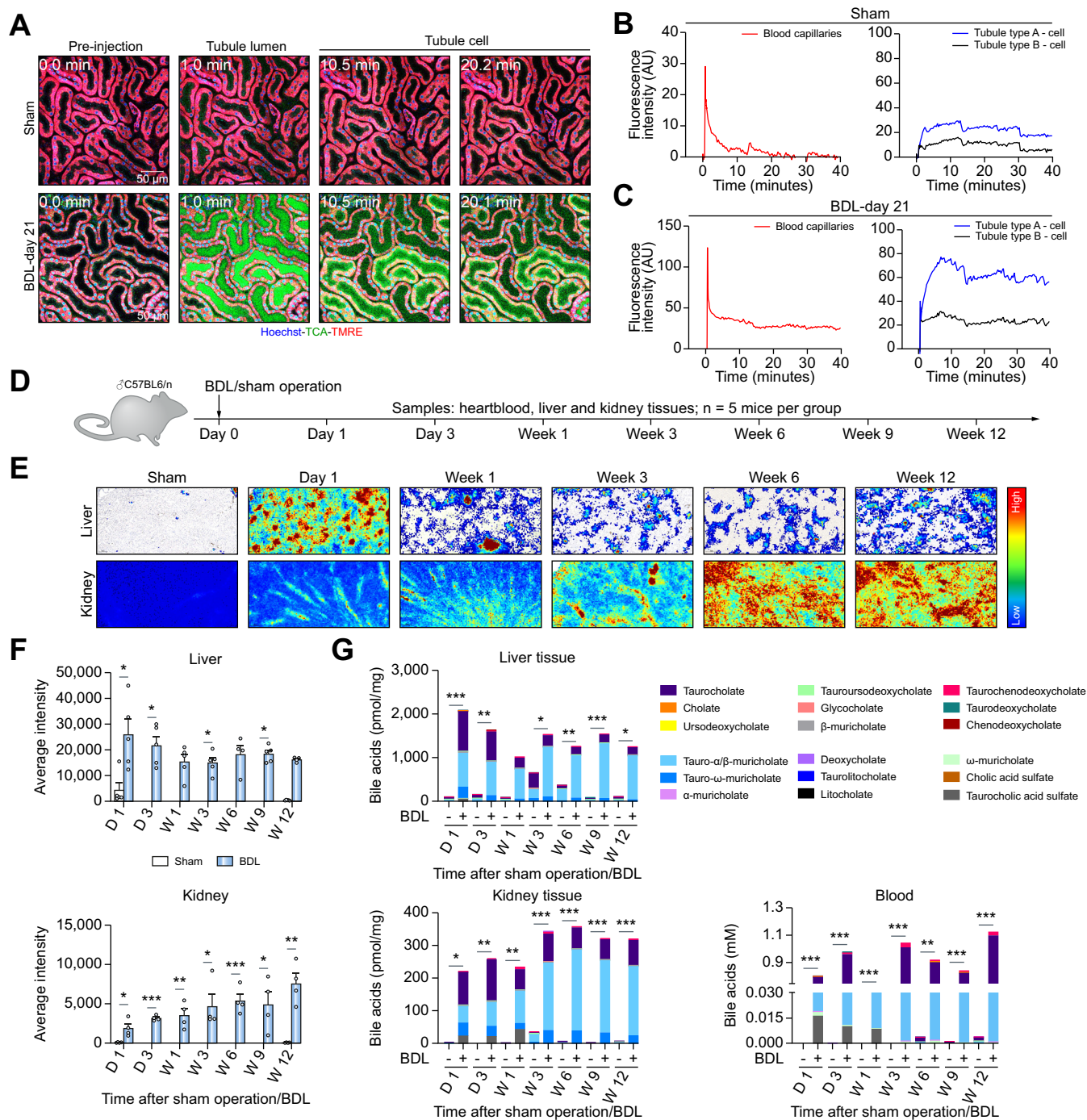
Fig. 1. Enhanced uptake of bile acids into renal tubular epithelial cells in obstructive cholestasis. (A-C) Stills from intravital videos of sham controls and mice 21 days after BDL, and corresponding quantifications. Red: TMRE; green: TCA; blue: Hoechst. Scale bars: 50 μm (Video S2). (D) Experimental schedule. (E,F). MALDI-MSI analysis of mouse livers and kidneys at different time intervals after BDL, and corresponding quantifications. (G) LC-MS/MS analysis of BAs in liver and kidney tissues and in blood; data are presented as mean± SEM; n = 5 mice per group. *p <0.05; **p <0.01; ***p <0.001 compared to sham day 1, Unpaired t test. The data are from male mice. BDL, bile duct ligation; TCA, taurocholic acid; TMRE, tetramethylrhodamine ethyl ester. (This figure appears in color on the web.)

Key events of CN: proximal TEC death and leakiness of peritubular capillaries

To study the consequences of chronic cholestasis on kidney function and morphology, kidney injury biomarkers in blood and urine, and kidney histopathology were analyzed time-dependently after BDL. Urea decreased in urine and increased in blood

(Fig. S4A, B). Bilirubin increased in blood and urine of BDL mice compared to controls (Fig. S4A, B). Creatinine concentrations decreased in urine while the urinary output increased (Fig. S4C). Macroscopically, a green discoloration of the kidneys was observed after BDL (Fig. S4D). H&E staining showed tubular cystic dilatation at week 1 after BDL, increasing thereafter, and at week 9 onwards, glomerular cysts were observed. Leukocyte infiltration

and Hall's positive casts occurred 3 days after BDL, with fibrosis appearing at week 6 and intensifying thereafter (Fig. S4D).

To differentiate proximal and distal tubules as well as collecting ducts, kidney tissue was co-immunostained for aquaporin (AQP)1, TSC (thiazide sensitive NaCl cotransporter) and AQP2 (Fig. 2A). Dilatation and casts were observed in the distal tubules and collecting ducts at day 3 and week 1, respectively, but not in proximal tubules. To understand the mechanism of this damage pattern, intravital imaging was performed using the oxidative stress marker H_2DCFDA (Fig. 2B; Fig. S5A). Proximal tubules were differentiated from distal tubules by their higher TMRE (tetramethylrhodamine, ethyl ester) intensity (Fig. S5A, B). As little as 4 h after BDL, oxidative stress was seen specifically in proximal TECs, which intensified until day one. This seemingly contradictory pattern, with dilatation and casts in distal TECs but oxidative stress in proximal TECs was further studied on intravital videos using the cytotoxicity marker SYTOX green and the mitochondrial marker TMRE. Already at day 1 after BDL, death of proximal but not distal TECs occurred (Figs 2C and S5B). The dead proximal TECs released cellular debris into the tubular lumen from where it floated downstream (Fig. 2C; Video S3A). Some of this detritus attached to the surface of distal tubules and collecting ducts forming casts and leading to dilatation (Fig. 2B,C; Video S3A). At week 3 after BDL, massive damage of renal tubules occurred, coinciding with green autofluorescence – possibly due to bilirubin – in and around peritubular capillaries (Figs 2B and S5A). To study if this autofluorescence is due to leaky capillaries, immunostaining of endothelial cells was performed using anti-MECA-32 antibodies. Severely compromised peritubular capillaries were observed particularly at week 3 after BDL and later (Fig. S6A). Intravital imaging was conducted using Evans blue, which under normal conditions does not leak from the capillaries.[17] As expected, Evans blue remained within the blood capillaries in sham-operated mice (Figs 2D,E and S6B; Video S4A). In contrast, 3 weeks after BDL, strong leakage was observed from peritubular capillaries into the interstitium (Figs 2D,E and S6B; Video S4B). At week 12, glomerular cysts manifested as dilatation of Bowman's space (Figs 2B and S5A; Video S3B). The imaging data corresponded to the time course of the proximal TEC marker KIM-1, which increased until week 1 before plateauing and decreasing thereafter (Fig. 2F); the proximal and distal TEC marker neutrophil gelatinase-associated lipocalin (NGAL) remained elevated until the end of the observation period, while the glomerular filtration marker cystatin C increased only at the longest periods of 9 and 12 weeks after BDL (Fig. 2F).

Identification of renal ASBT as a possible therapeutic target in CN

As shown above, BA enrichment in proximal TECs is a key early event in CN progression. The main carrier responsible for reabsorption of the non-sulfated BAs in TECs is ASBT[18] (Fig. 3A). In contrast to the adaptive changes of BA transporters in the liver (Fig. S7), renal *Asbt* expression was not significantly downregulated up to 6 weeks after BDL (Fig. 3B). Renal multidrug resistance-associated protein (MRP)2, which pumps BAs into the tubular lumen, was only moderately altered, whereas MRP4, which also exports BAs at the luminal apical membrane, was significantly upregulated (Fig. 3C). Interestingly, the basolateral BA exporters MRP3 and OSTα (organic solute transporter alpha) were significantly upregulated after BDL

(Fig. 3D), suggesting that BAs may be more efficiently exported into the interstitium, from where they can reach the peritubular capillaries. In agreement with the RNA analysis, immunostaining of ASBT in the kidneys of mice after BDL did not show major changes compared to controls (Fig. 3E). Expression of ASBT occurred at the luminal side of TECs and was exclusively observed in AQP1-positive cells, a marker of proximal tubules (Fig. S8A). This is consistent with the functional analysis where fluorophore-coupled TCA showed a mosaic pattern with tubules that either do or do not reabsorb BAs (Fig. S8B). MALDI-MSI analysis of TCA supported the selective enrichment of TCA in ASBT-positive proximal TECs (Fig. S8C).

To study the translational relevance of the preserved ASBT expression in kidneys of cholestatic mice, a set of kidney biopsies from patients with early and advanced stages of CN, identified based on histopathological examination, was analyzed. Importantly, ASBT expression was preserved in patients with CN even at the late stages of the disease (Fig. 3F).

Evaluation of a systemic ASBT-specific inhibitor

To investigate the possible role of renal ASBT in the development of CN, we performed intervention studies with the novel compound AS0369 which has an IC_{50} of 1.31 nM for mouse ASBT and has >100-fold greater specificity for mouse ASBT *vs.* mouse NTCP (sodium-taurocholate co-transporting polypeptide) (Fig. 4A). After administration of 10 mg/kg AS0369 (per os) to wild-type mice, the mean C_{max} in blood was 222 nM (Fig. 4A; Fig. S9A) and the half-life was 2 h. Appreciable levels of AS0369 were also found in kidney tissue and in urine (Fig. 4A). To test the efficacy of AS0369 in the inhibition of renal ASBT *in vivo*, a pilot experiment was designed using female mice to allow for repeated urine collection by a urinary bladder catheter. Starting from day 7 post-BDL, the mice received various doses of AS0369 (15-120 mg/kg) orally twice per day for 5 days (Fig. 4B). Urine samples were collected daily, and blood samples were obtained 4-7 h post-dosing at day 5 for determination of plasma AS0369 and BA concentrations (Figs 4B and S9B). The lowest dose tested (15 mg/kg) increased urinary excretion of non-sulfated BAs (Fig. 4C). In contrast, little effect was observed on sulfated BAs, which are poor substrates of ASBT. Plasma concentrations of BAs were reduced with all tested doses of AS0369, but doses of 30-120 mg/kg were more effective than 15 mg/kg (Fig. 4D).

For a further pilot experiment with intravital imaging, a dose of 60 mg/kg AS0369 was selected; this dose evoked excessive increases in urinary BAs and was well tolerated. Interestingly, twice daily administration of AS0369 for 2 days, beginning on the day of BDL, strongly reduced the uptake of TCA into TECs (Fig. 4E), ameliorated oxidative stress in proximal TECs and tubular casts in distal tubules compared to vehicle-treated BDL mice (Fig. 4F). Therefore, a dose of 60 mg/kg was used for comprehensive efficacy studies.

### Efficient prevention of CN by inhibition of renal ASBT

To evaluate the efficacy of AS0369 in the prevention of CN, a study design with female mice subjected to BDL and simultaneously treated with AS0369 (60 mg/kg, twice daily) or with vehicle for 6 weeks was performed. Sham-operated mice treated with vehicle served as controls (Fig. 5A). Treatment with AS0369 prevented mortality throughout the study period
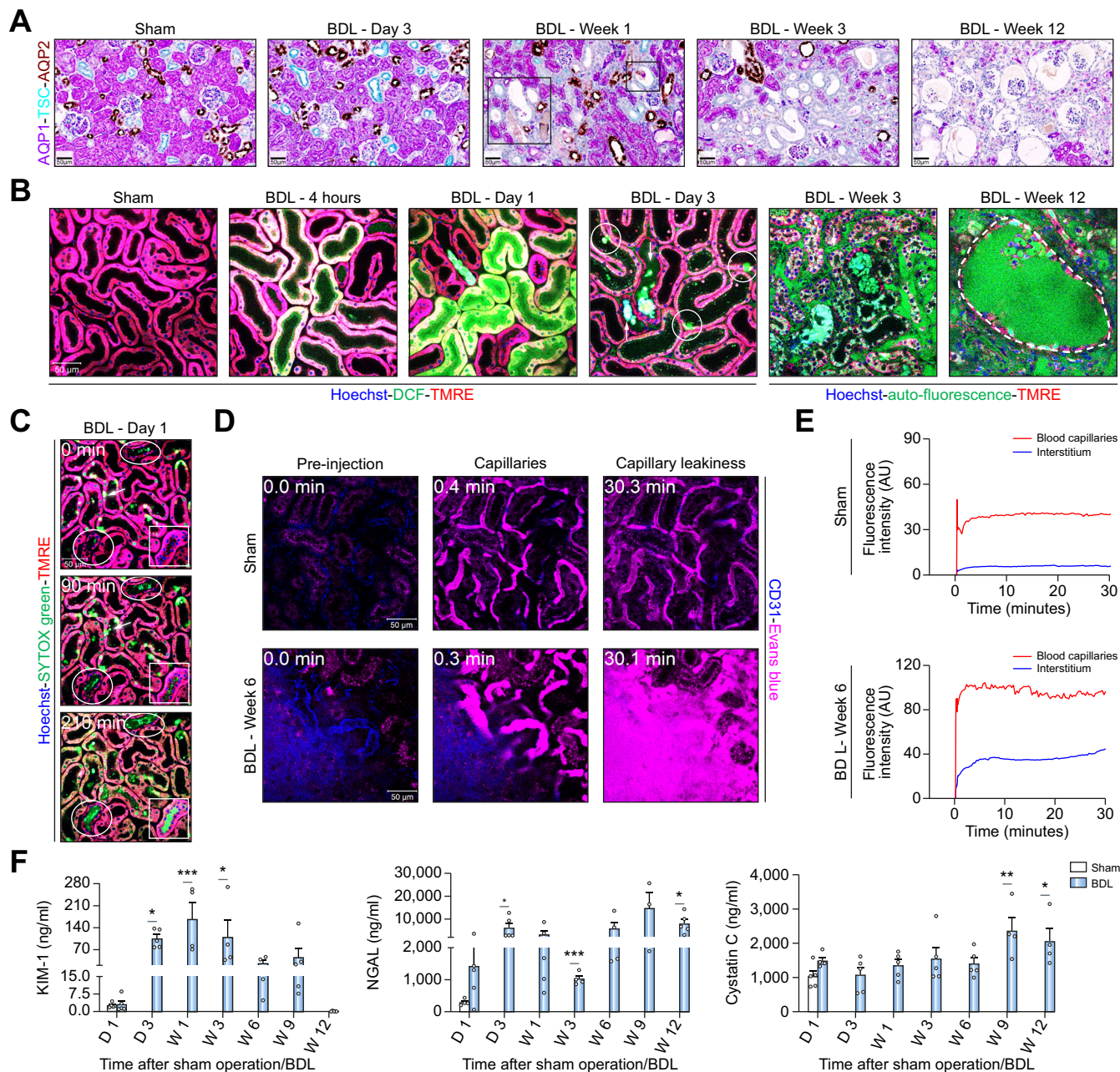
Fig. 2. Key events of CN. (A) Co-immunostaining of the proximal TEC marker AQP1, distal TEC marker TSC and the collecting duct marker AQP2 at various time periods after BDL. (B) Intravital imaging demonstrating oxidative stress of proximal TECs 4 h and 1 day after BDL based on the marker DCF. Dead proximal TECs (circles) and debris attached in distal tubules (arrows) on day 3 after BDL. Auto-fluorescence in (white arrows) and around peritubular capillaries at week 3 post BDL. Week 12 after BDL shows glomerular cysts (marked area). (C) Intravital imaging of dead proximal TECs based on the cytotoxicity marker SYTOX Green (arrowhead) at day 1 after BDL and formation of casts in a collecting duct (square) and distal tubules (circles) (Video S3A). (D) Leakiness of peritubular capillaries 6 weeks after BDL. Intravital imaging was performed after tail vein injection of Evans blue (magenta). Peritubular capillaries are visualized by anti-CD31 antibody (blue); scale bars: 50 μm. (E) Quantification of Evans blue signal in the peritubular capillaries and in the interstitium corresponding to Video S4. (F) Time course of kidney injury biomarkers in urine; data are presented as mean ± SEM; n = 5 mice per group. *p <0.05; **p <0.01; ***p <0.001 compared to the corresponding sham controls; Tukey's multiple comparisons test. The data are from male mice. BDL, bile duct ligation; D, day; DCF, dichlorofluorescein; TKIM1, kidney injury molecule; MRE, tetramethylrhodamine ethyl ester; NGAL, neutrophil gelatinase-associated lipocalin; W, week. (This figure appears in color on the web.)

compared to ~50% mortality in the vehicle-treated BDL group (Fig. 5B). In addition, BDL-induced body weight loss was prevented by treatment with AS0369 (Fig. 5C). The apparent body weight recovery in the BDL vehicle group by 6 weeks may be due in part to a dramatically increased gallbladder volume (Figs 5D,E and S10A). The BDL-associated increase in gallbladder volume was reduced by AS0369 (Fig. 5E). Furthermore, kidneys with a normal reddish-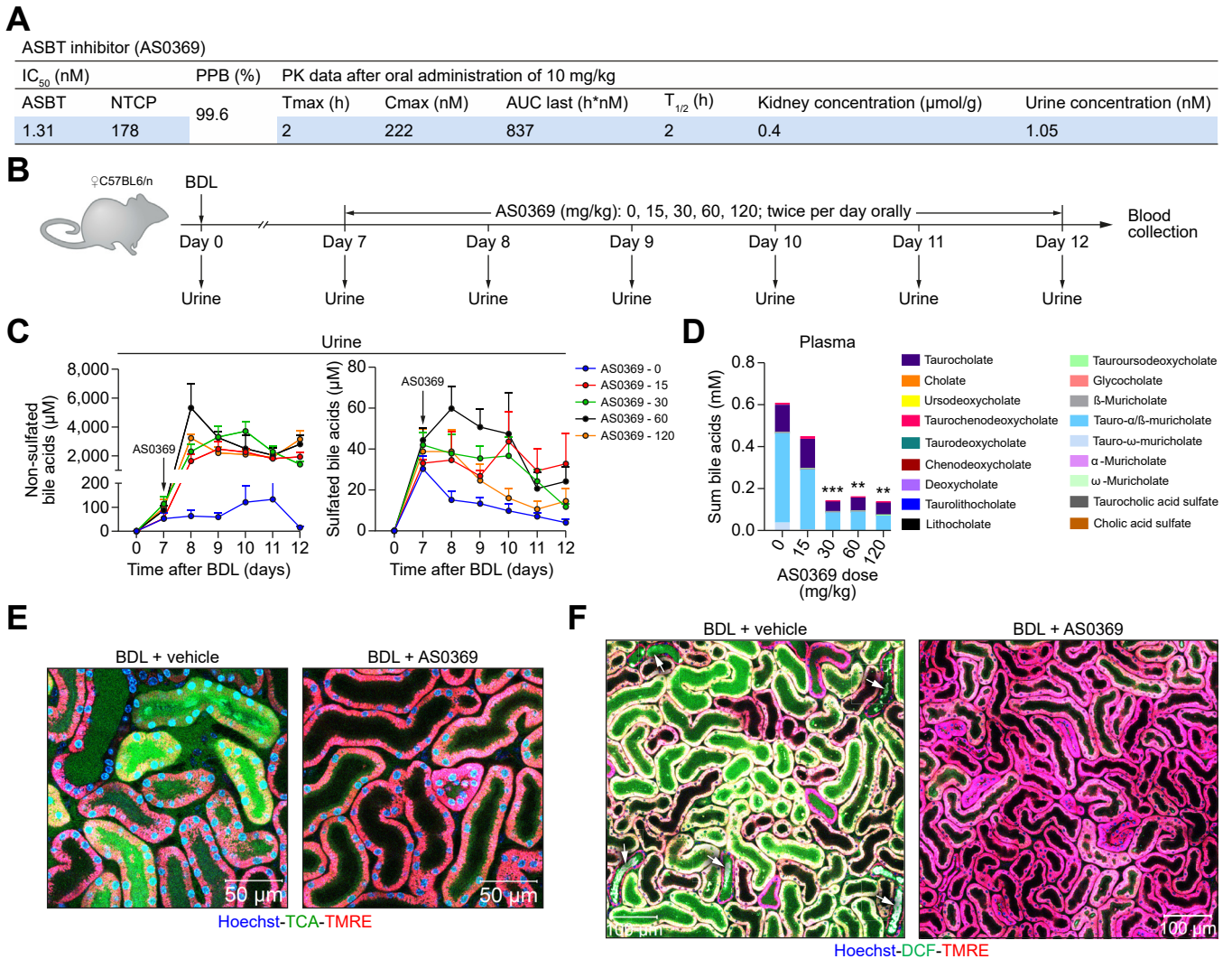brown gross morphology were observed in the AS0369-treated BDL mice compared to kidneys with a greenish discoloration in the BDL vehicle group (Fig. 5D). The kidney-to-body weight ratio was not significantly altered in all groups, but the liver-to-body weight ratio showed a significant increase in the BDL vehicle group compared to the sham controls, which was ameliorated by AS0369 (Fig. S10B,C).
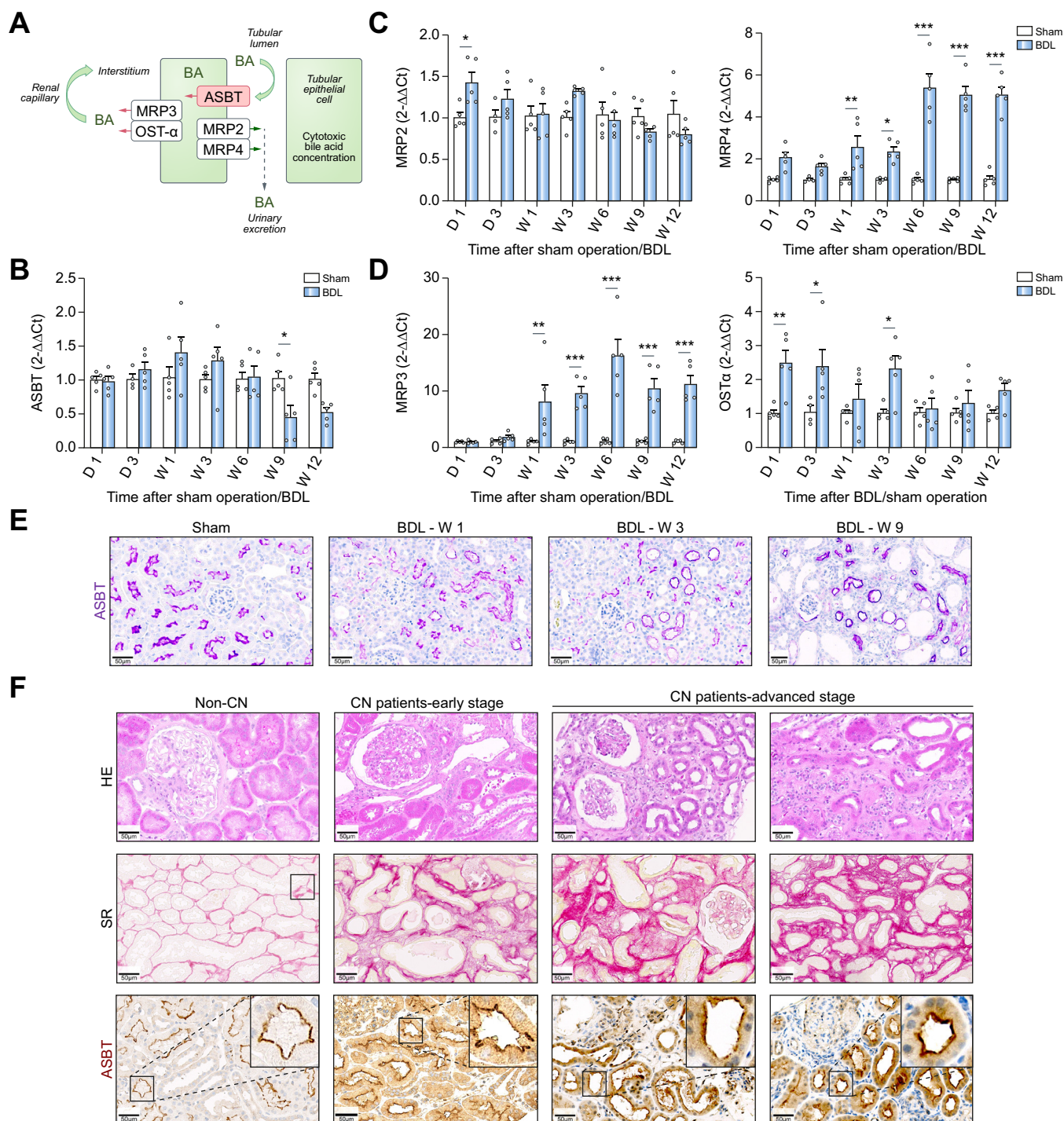
Fig. 3. Preserved ASBT expression in renal tissue of mice and patients with CN. (A) Schedule of BA transport in TECs. (B-D) RNA levels of BA transporters in renal tissue of mice at various periods after BDL compared to sham-operated mice; data are presented as mean ± SEM; n = 5 mice per group; *p <0.05; **p <0.01; ***p <0.001 compared to the corresponding controls; Tukey's multiple comparisons test. (E) Immunostaining of ASBT in renal tissue of mice after BDL. The data are from male mice. (F) ASBT expression in renal biopsies of patients with CN at early and advanced stages. Fibrosis was visualized by Sirius red (SR). Scale bars: 50 μm. ASBT, apical sodium-dependent bile acid transporter; CN, cholemic nephropathy; HE, haematoxylin and eosin; Mrp2/3/4, multidrug resistance-associated protein 2/3/4; Ostα, organic solute transporter alpha; SR, sirius red. (This figure appears in color on the web.)

Next, the effect of systemic ASBT inhibition with AS0369 on BA concentrations in relevant compartments was investigated. Urinary and renal tissue BA concentrations in the sham controls were very low, while they were elevated in response to BDL (Fig. 5F). Nonetheless, BA concentrations in urine were massively increased in the AS0369-treated *vs.* vehicle-treated BDL mice and were strongly reduced in liver and kidney tissue and in blood, whereas BA concentrations in bile were slightly increased (Fig. 5F). In agreement, MALDI-MSI analysis of TCA in liver and kidney tissues showed a strongly reduced signal in the

A

ASBT inhibitor (AS0369)

IC$_{50}$ (nM)		PPB (%)	PK data after oral administration of 10 mg/kg					
ASBT	NTCP	99.6	Tmax (h)	Cmax (nM)	AUC last (h*nM)	T$_{1/2}$ (h)	Kidney concentration (µmol/g)	Urine concentration (nM)
1.31	178		2	222	837	2	0.4	1.05

**B**

C

D

E

F

Fig. 4. Development of a systemic ASBT-specific inhibitor. (A) Inhibitory concentrations and pharmacokinetic data for AS0369. (B) Experimental schedule. (C, D) Concentrations of non-sulfated and sulfated BAs in urine and plasma after ASBT inhibition; data are presented as mean ± SEM; n = 3-6 mice per group; **p <0.01; ***p <0.001 compared to the controls (0); Tukey's multiple comparisons test. (E) ASBT inhibition reduces TCA uptake into TECs. Intravital imaging was performed 3 days after BDL and AS0369 treatment (60 mg/kg, twice per day). Imaging was performed approximately 2 h after administration of the last AS0369 dose; scale bars: 50 µm. (F) Overview of renal tissue in mice on day 2 after BDL showing reduced oxidative stress and tubule casts after AS0369 treatment compared to vehicle treated mice; scale bars: 100 µm. The data in panels (E) and (F) are from male mice. ASBT, apical sodium-dependent bile acid transporter; BDL, bile duct ligation; DCF, dichlorofluorescein; NTCP, sodium-taurocholate co-transporting polypeptide; PPB, plasma protein binding; PK, pharmacokinetic; TCA, taurocholic acid; TMRE, tetramethylrhodamine ethyl ester. (This figure appears in color on the web.)

AS0369-treated mice compared to the BDL vehicle-treated group (Fig. 5G, H; Fig. S11). Treatment with AS0369 significantly reduced total serum bilirubin, alkaline phosphatase, and blood urea nitrogen, but not the liver damage biomarkers alanine and aspartate aminotransferase (Fig. 5I). AS0369 particularly reduced the TEC damage biomarker NGAL in urine (Fig. 5J). To study the effect of AS0369 at the tissue level, histological analysis of the kidney was performed. A strong reduction in leukocyte infiltration, fibrosis, tubule damage, cast formation, and endothelial cell damage was observed in the AS0369-treated BDL mice compared to vehicle-treated BDL mice (Figs 6A,B, S12 and 13A). In agreement, expression of early growth response protein 1, which plays a critical role in kidney fibrogenesis, was upregulated in kidney tissue after BDL and reduced to control levels by AS0369 (Fig. 6C). Furthermore, vascular

leakage of Evans blue into the interstitium of kidney tissue after BDL was almost completely prevented by AS0369 (Figs 6D,G and S13B; Videos S5A-C). Sirius red staining of the liver showed periportal and perisinusoidal fibrosis in the vehicle treated BDL mice (Fig. S14). Treatment with AS0369 reduced the perisinusoidal fibrosis, and ameliorated canalicular dilatation (Fig. S14).

Next, the influence of ASBT inhibition on BA carrier expression in the liver and kidney and *Cyp7a1* expression in the liver was analyzed. AS0369 treatment did not significantly alter expression of the BA carriers in the liver compared to the BDL vehicle group, except that the BDL-induced upregulation of MRP4 was ameliorated in response to AS0369 (Fig. S15A). However, *Cyp7a1* expression was upregulated after AS0369 treatment (Fig. S15A). In kidney tissue, AS0369 treatment
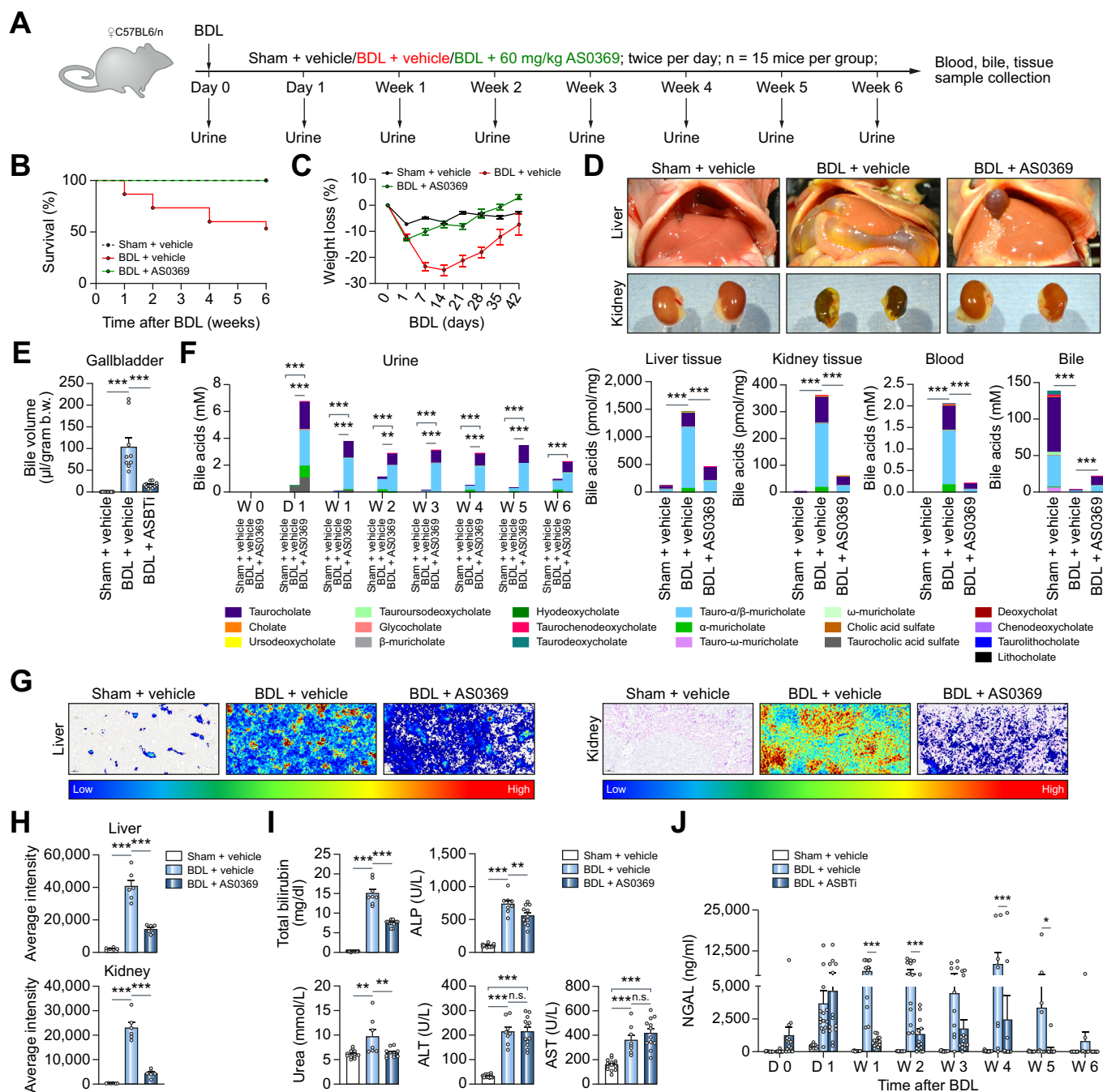
Fig. 5. Efficient prevention of CN by inhibition of renal ASBT. (A) Experimental schedule. (B, C) Survival analysis and body weight changes. (D) Gross pathology of mouse livers and kidneys. (E) Gallbladder bile volume. (F) BA concentrations in urine, liver, and kidney tissues, blood, and bile. ***p <0.001, Tukey's multiple comparisons test. (G, H) MALDI-MSI analysis of taurocholic acid in liver and kidney tissues, and corresponding quantifications. (I, J) Blood (total bilirubin, alkaline phosphatase, urea, ALT, AST) and urine (NGAL) biomarkers of liver and kidney damage. *p <0.05, ***p <0.001, Tukey's multiple comparisons test. Data are presented as mean ± SEM. The data are from female mice. ALP, alkaline phosphatase; ALT, alanine transaminase; AST, aspartate transaminase; BDL, bile duct ligation; NGAL, neutrophil gelatinase-associated lipocalin. (This figure appears in color on the web.)

prevented the BDL-induced dysregulation of BA carrier expression except for MRP4 (Fig. S15B).

Since the main intervention study was performed in female mice, we repeated the intervention experiment using male mice, with the difference that urine was only collected at the end of the 6-week treatment. The results confirmed the remarkable protection against development of CN conferred by AS0369 and showed that this effect is not sex specific (Figs S16 and S17).

RNA-sequencing reveals large effect size of ASBT inhibition

To perform an unbiased evaluation of the effect of ASBT inhibition at the transcriptional level, kidney and liver tissues were analyzed by RNA-sequencing. The kidney samples from BDL mice treated with AS0369 clustered closer to controls than to vehicle-treated BDL mice in a principal component analysis (Fig. 7A), indicating a sizable effect of AS0369 treatment in the kidney, which was also reflected by many significantly up and
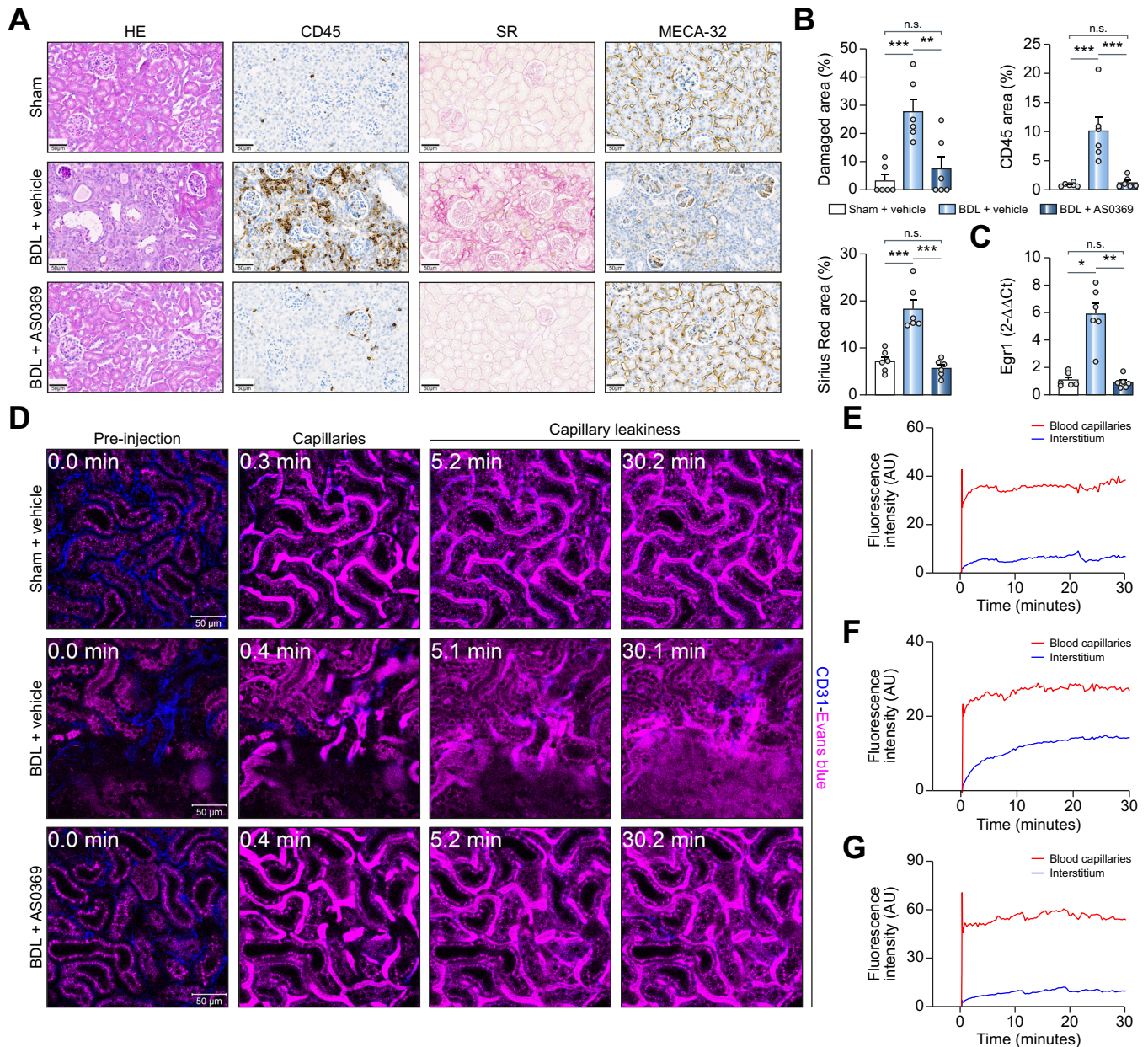
Fig. 6. Prevention of peritubular capillary leakiness by ASBT inhibition. (A,B) Histopathology and immunostaining of leukocyte (CD45), and endothelial cells (MECA-32) in the three treatment groups illustrated in Fig 5A, and corresponding quantifications; scale bars: 50 μm. (C) RNA levels of *Egr1* in renal tissue; *p <0.05, **p <0.01, ***p <0.001; Tukey's multiple comparisons test. Data are presented as mean ± SEM. (D-G) Intravital imaging after tail vein injection of Evans blue (magenta) and the corresponding quantifications in the peritubular capillaries and the interstitium (Videos S5A-C). The peritubular capillaries are visualized by anti-CD31 antibody (blue); scale bars: 50 μm. The data are from female mice. BDL, dile duct ligation; CD45, cluster of differentiation 45, Egr1, early growth response protein-1; HE, haematoxylin and eosin; MECA-32, mouse endothelial cell antigen-32; SR, sirius red. (This figure appears in color on the web.)

downregulated genes (Fig. 7B). To further investigate this effect, genes were plotted by their log2-fold-changes over controls for vehicle-treated (x-axis) and AS0369-treated (y-axis) BDL mice (Fig. 7C), delineating five gene groups: genes in group 1a and 2a were upregulated by BDL and downregulated by AS0369, either completely to control levels (1a) or partially (2a). Conversely, genes in 1b and 2b were downregulated in response to BDL, which was either completely (1b) or partially (2b) prevented by AS0369. Only relatively few genes were induced by AS0369 treatment but not affected by BDL, representing AS0369-specific response genes (3a). Overrepresentation analysis demonstrated an enrichment in inflammation-associated gene

ontology groups for genes upregulated due to BDL, while the downregulated genes were associated with metabolic processes (Fig. 7D). Correspondingly, genes upregulated by BDL and downregulated to control levels by AS0369 (1a) were also inflammation-associated, and genes downregulated by BDL and increased to control levels by AS0369 (1b) also represented metabolic gene ontology groups (Fig. 7E). The most downregulated gene upon ASBT inhibition in group 1a was the extracellular matrix protein COL10A1, and the most upregulated gene in group 1b was histidine decarboxylase, which catalyzes the synthesis of histamine (Fig. 7F). Qualitatively similar consequences of ASBT inhibition were observed in the livers of the

same mice, but the effect was smaller (Fig. 7G-L). Nevertheless, the overlaps of altered genes in the liver and kidney were higher than randomly expected (Fig. S18). Altogether, the RNA-sequencing analysis demonstrated that AS0369 treatment ameliorated BDL-induced gene expression in the kidney, while the effects in the liver were smaller.
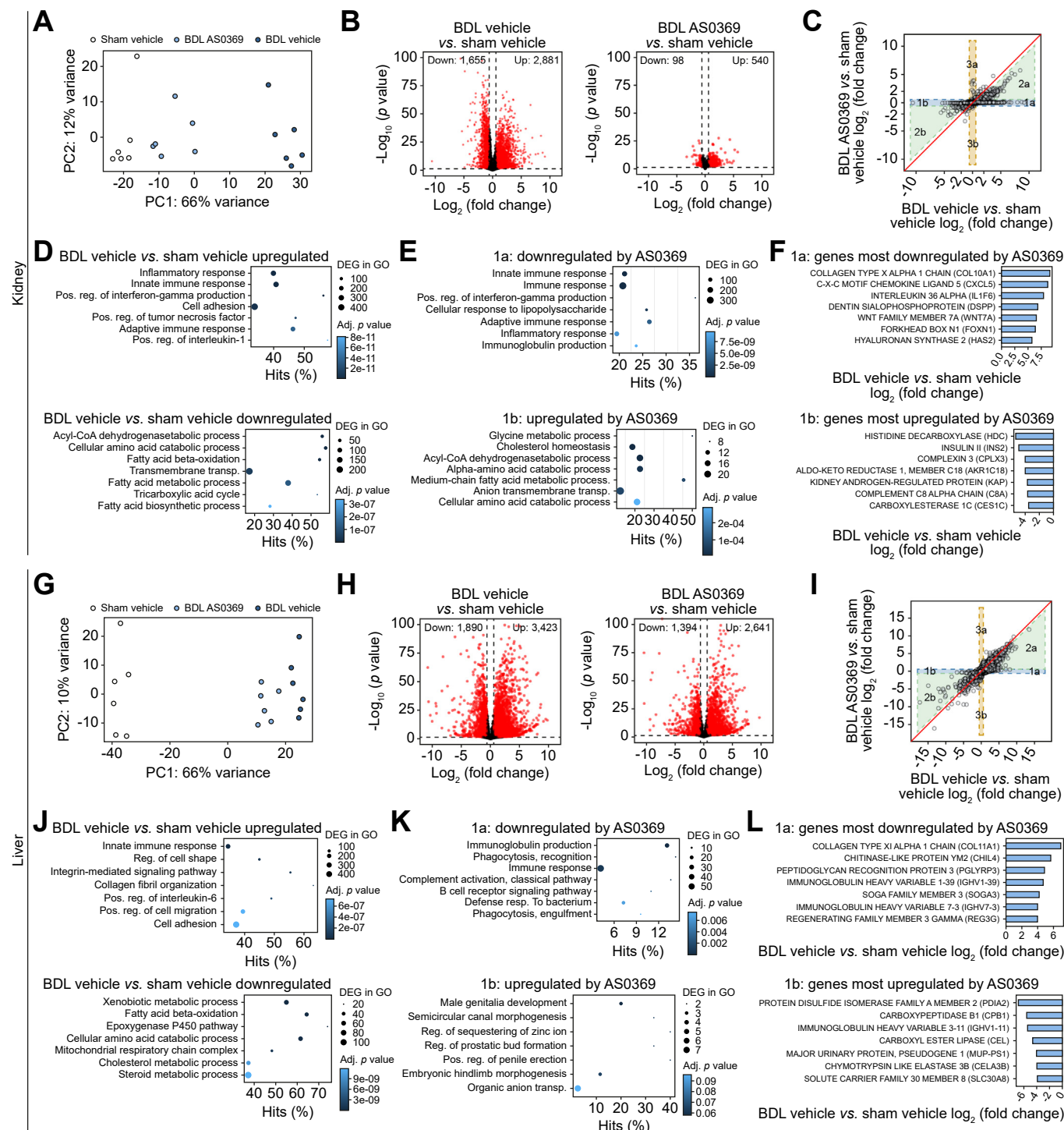
Fig. 7. RNA-seq analysis of BDL mice confirms the protective effect of ASBT inhibition in the kidney and liver. (A) PCA plots of sham vehicle mice, BDL mice treated with the vehicle, and BDL mice treated with AS0369. Each dot represents an individual mouse. (B) Volcano plots illustrating differential genes between vehicle-treated (left panel) and AS0369-treated (right panel) mice with BDL and controls (sham vehicle). (C) DiPa plots illustrating the response to AS0369. Each dot represents an individual gene. (D, E) Plots of overrepresented GO groups in the indicated differential gene sets. The size of the dots represents the number of genes in the individual GO groups and the color code the adjusted (adj) *p* value. (F) Genes most influenced by AS0369 in groups 1a and 1b of the DiPa plot. (G-L) correspond to A-F but were performed with liver tissue. The data are from female mice. BDL, bile duct ligation; PCA, Principal component analysis. (This figure appears in color on the web.)

Translational relevance

Large differences in BA synthesis and composition are known between humans and mice. Therefore, we used the *Cyp2c70*^{-/-} mice with humanized BA spectrum[19] that – like humans – have lower total BAs but higher concentrations of the more toxic BA chenodeoxycholic acid, and very low levels of hydrophilic muricholate BA (Fig. 8A-C). AS0369 also increased sum BA concentrations in the urine of the *Cyp2c70*^{-/-} mice (Fig. 8A), including BAs that are formed by humans but not (or only at very low concentrations) by mice, such as taurochenodeoxycholic acid (Fig. 8B). Upon BDL, *Cyp2c70*^{-/-} mice showed aggravated kidney injury compared to wild-type mice, as illustrated by higher levels of NGAL (Fig. 8C). *Cyp2c70*^{-/-} mice could not be analyzed for periods longer than 24 h after BDL, because of their poor health status that was much worse compared to that of wild-type mice. It took about 1 week for AS0369 to reduce NGAL in WT mice after BDL (Fig. 5J). However, in *Cyp2c70*^{-/-} mice, a significant reduction in NGAL was already seen at day 1 in male mice, with a trend in female mice (Fig. 8C). Thus, AS0369 also enhances urinary excretion of a humanized and more hydrophobic spectrum of BAs and ameliorated BDL-induced kidney injury.

To address the translational relevance of the findings in mice, we studied patients with acute and/or chronic liver disease with serum bilirubin >6 mg/dl (n = 67) and healthy volunteers (n = 36) and focused on the relationship between sum BA and bilirubin concentrations in serum and the proximal TEC damage marker KIM-1 (patient characteristics: Table S1B). Besides liver enzymes, bilirubin, and BA, blood urea nitrogen, cystatin C, NGAL, and KIM-1 were significantly increased in patients compared to healthy volunteers (Fig. 8D). Among patients with acute and/or chronic liver disease, sum BA concentrations correlated positively with bilirubin levels (Fig. 8E) and both bilirubin and BA correlated positively with KIM-1 (Fig. 8F,G). In a multiple linear regression model after backward selection, only sum BA was kept as an explanatory variable for KIM-1, while bilirubin, C-reactive protein (a marker of systemic inflammation, which may contribute to kidney injury), and ursodeoxycholic acid therapy were excluded (Fig. 8H).

Discussion

The mechanisms of CN pathogenesis remain poorly understood, and no specific treatments are available.[3,6] Therefore, we studied the pathomechanisms of BDL-induced CN in mice by intravital imaging and observed five subsequent events: i. BA increase in blood and enrichment in proximal TECs (almost immediately after BDL); ii. oxidative stress in proximal TECs (4 h onwards); iii. death of proximal TECs with release of debris into the tubular lumen, which travels downstream and forms casts in the distal tubules and collecting ducts, followed by dilatation of tubules (day 1-3 onwards); iv. peritubular capillary damage and leakiness (week 3 onwards); and v. glomerular cysts (week 6 onwards).

ASBT is known to transport BAs from the tubular lumen into TECs. Therefore, to study a possible causal relationship between BA enrichment and oxidative stress, as well as cell death of proximal TECs, we utilized the systemically bioavailable specific ASBT inhibitor, AS0369, which blocked the uptake of BAs into TECs almost completely. A remarkable finding was the

large effect size of AS0369, and the renal protective effects associated with decreasing kidney BA levels. All CN hallmarks (event i-v) were almost completely absent with twice daily AS0369 administration over a 6-week period after BDL.

Targeting renal ASBT not only provides renal protective effects but also serves as a means of lowering overall BA load in the body by increasing urinary excretion. Indeed, plasma BA concentrations decreased strongly in response to AS0369. Importantly, the elevated urine BA levels induced by AS0369 also offer a non-invasive biomarker of renal ASBT target engagement which may have translational value. Plasma levels of AS0369 dosed at 60 mg/kg were approximately 200 nmol/L 4-7 h after administration. Since AS0369 is tightly protein bound (>99%), free plasma levels were approximately 1-2 nmol/L which equates to the ASBT IC_{50}, suggesting that the observed efficacy was not due to off-target interactions.

While TEC death occurred within the first days after BDL (event i-iii), compromised capillary endothelial cells were observed at week 3 onwards (event iv). This led to peritubular capillary leakage and is possibly explained by endothelial cell damage caused by an elevated flux of BAs from the tubule lumen into the interstitial space, although elevated circulating BAs could also contribute. Nonetheless, AS0369 treatment substantially improved renal peritubular capillary integrity.

The protective effect of AS0369 in the kidneys was also reflected in the genome-wide analyses, where AS0369 reduced the number of genes deregulated by BDL to a larger degree in the kidney than the liver. A plausible explanation for the stronger effect in the kidney is that TECs are specifically protected against BA overload by AS0369, since ASBT appears to be the sole mechanism for reabsorption of non-sulfated BAs from the tubule lumen. Conversely, hepatocytes continue to synthesize BAs and AS0369 does not affect hepatocellular sinusoidal BA uptake via NTCP and OATPs (organic anion transporting proteins). As such, the liver BA content remains elevated above normal levels in this model of complete biliary tract obstruction. These findings generally agree with a recently published study, where whole body ASBT knockout mice showed decreased liver damage 5 days after BDL.[20] In addition, administration of an intestine-restricted ASBT inhibitor in combination with the farnesoid X receptor agonist obeticholic acid lowered the BA pool, and ameliorated liver injury 2-days post-BDL.[20]

Systemic ASBT inhibition has multiple favorable consequences in advanced liver diseases. Blocking renal ASBT specifically protects a subset of TECs that are vulnerable to BA toxicity and prevents CN (so-called organ-protection). Moreover, increased urinary elimination of non-sulfated BAs, which lowers the overall BA pool, is favorable for all cell types compromised by exposure to high levels of circulating BAs. Importantly, in *Cyp2c70*^{-/-} mice, that have a humanized BA composition,[19] we observed that AS0369 also enhanced urinary excretion of the more toxic hydrophobic BAs, such as taurochenodeoxycholic acid, and ameliorated kidney injury after BDL, indicating a possible human relevance.

An initial key event of CN in mice is the accumulation of BAs in proximal TECs, cell death and the release of KIM-1 from this cell type. Since KIM-1 is also considered a marker of proximal TEC injury in humans,[2] we analyzed KIM-1 in serum of patients with acute and/or chronic liver disease and hyperbilirubinemia. The sum BA concentration was the key explanatory variable in
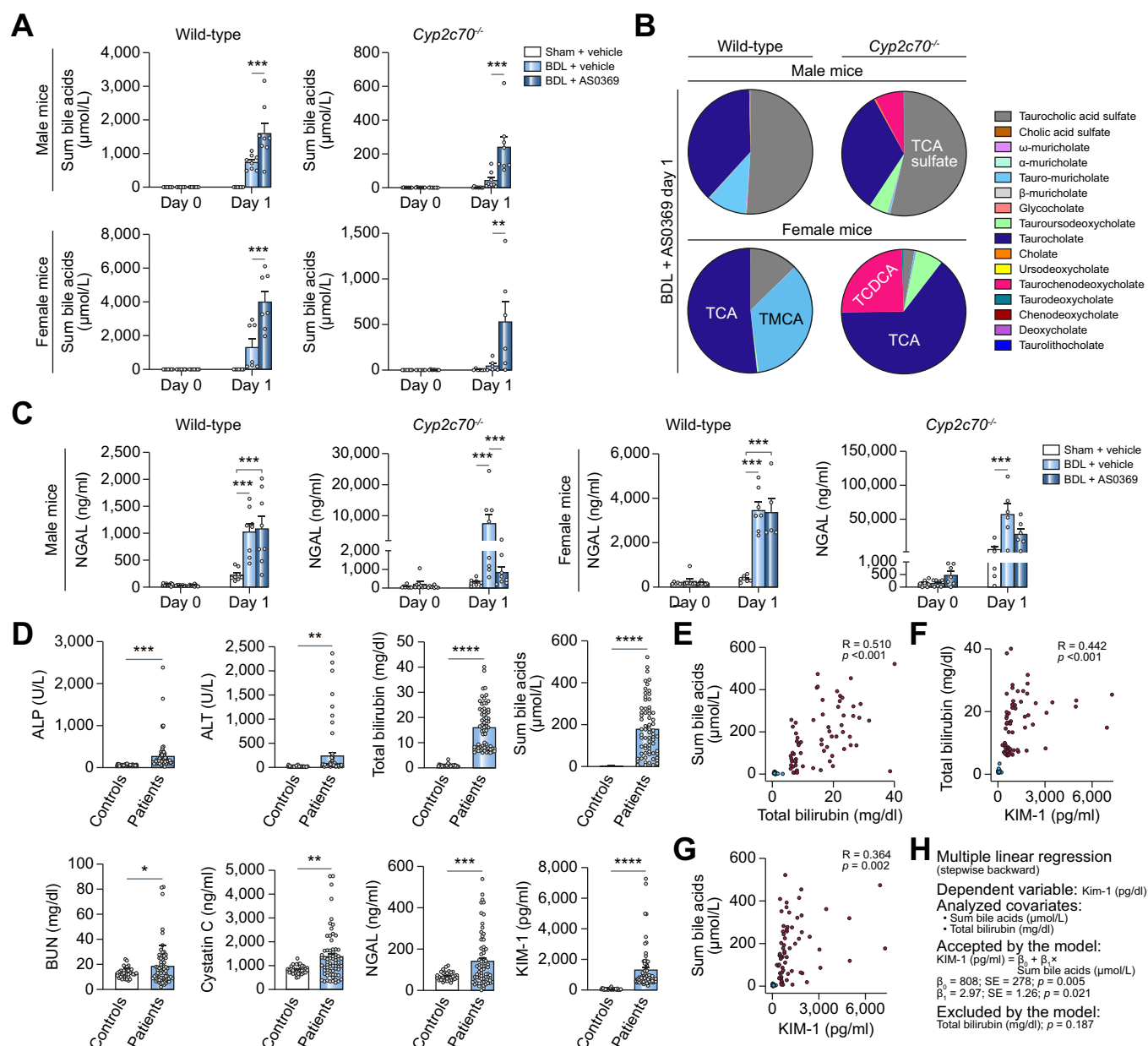
Fig. 8. Translational relevance. (A-C) Analysis of mice with humanized BA spectrum; *Cyp2c70*^{−/−}. (A) Urine BAs in mice after sham surgery, BDL and vehicle administration, and BDL plus 60 mg/kg AS0369 twice, on day 1. (B) Individual BAs in wild-type and *Cyp2c70*^{−/−} mice. (C) Urine NGAL in male and female wild-type and *Cyp2c70*^{−/−} mice. **p <0.01, ***p <0.001; Tukey's multiple comparisons test. (D-H) Analysis of patients with acute and/or chronic liver disease and hyperbilirubinemia. (D) Liver enzymes, bilirubin, BA and kidney injury markers in serum of patients and in healthy volunteers (controls). *p <0.05, **p <0.01, ***p <0.001, ****p <0.0001; Unpaired t-test. (E-G) Spearman's correlation of BA, bilirubin, and KIM-1 in serum of patients (red circles) and heathy volunteers (blue circles); R: correlation coefficient; P: Spearman's p value. (H) Multiple linear regression analysis with serum KIM-1 as a dependent variable. ALP, alkaline phosphatase; ALT, alanine transaminase; BDL, bile duct ligation; BUN, blood urea nitrogen; KIM1, kidney injury molecule; NGAL, neutrophil gelatinase-associated lipocalin. (This figure appears in color on the web.)

a multiple linear regression model with KIM-1 as the dependent variable, suggesting that BAs may play a pivotal role in human kidney injury in the context of liver dysfunction. The present human data does not exclude that bilirubin (and possibly additional cholephiles released from the liver) may be relevant, considering that patients were selected based on a cut-off of >6 mg bilirubin/dl. The latter was chosen as it denotes liver dysfunction in the context of decompensated cirrhosis[4] and an analysis of 1,372 patients included in the above-mentioned registry study found that profound elevations of BA are uncommon in patients with lower bilirubin values (data not shown). Notably, mean arterial pressure (as a marker of circulatory dysfunction) was not included in our models, as all bar two patients with mean arterial pressures of 64 mmHg had pressures ≥65 mmHg and C-reactive protein (as a marker of systemic inflammation) was less closely associated with proximal TEC injury than sum BA concentration.

At first glance, it may be surprising that the earliest key events of CN occur in proximal tubules in the present mouse study, as casts are observed in distal tubules in human biopsies.[2] The herein described mechanism resolves this discrepancy, since debris from dead proximal TECs travels

downstream in the tubule lumen to induce cast formation in distal tubules and collecting ducts; compartments with a high luminal osmolarity. In biopsies only the latter cast formation but not the initial death events in proximal TECs can be detected. A further translationally relevant component of the herein described mechanisms is that ASBT expression is preserved in patients with CN at the luminal side of proximal TECs.

In conclusion, a mouse model of CN identified BA enrichment in TECs as a critical pathomechanism. Blocking renal ASBT-mediated BA reabsorption prevented CN development and systemically decreased BA concentrations. Taken together, systemically available ASBT inhibitors reaching the kidney may exert reno-protective effects in conditions of kidney injury secondary to liver disease.

Affiliations

[1]Department of Toxicology, Leibniz Research Centre for Working Environment and Human Factors, Technical University Dortmund, Ardeystr. 67, 44139 Dortmund, Germany; [2]Department of Forensic Medicine and Toxicology, Faculty of Veterinary Medicine, South Valley University, 83523 Qena, Egypt; [3]Albireo Pharma, Inc., Boston, MA 02109, USA; [4]Dr. Margarete Fischer-Bosch Institute of Clinical Pharmacology and University of Tübingen, Auerbachstr. 112, 70376 Stuttgart, Germany; [5]Department of Statistics, TU Dortmund University, 44227 Dortmund, Germany; [6]Institute of Computer Science & Saxonian Incubator for Clinical Research (SIKT), University of Leipzig, Haertelstraße 16-18, 04107 Leipzig, Germany; [7]Department of Gastroenterology, Hepatology and Infectious Diseases, University Hospital Duesseldorf, Medical Faculty at Heinrich-Heine-University, 40225 Dusseldorf, Germany; [8]Histology Department, Faculty of Medicine, South Valley University, 83523 Qena, Egypt; [9]Department of Pharmacology, Faculty of Veterinary Medicine, Sohag University, 82524 Sohag, Egypt; [10]Department of Pharmacology, Faculty of Veterinary Medicine, South Valley University, 83523 Qena, Egypt; [11]Department of Biomedical Sciences, An-Najah National University, P.O. Box 7 Nablus, Palestine; [12]Department of Pharmacy, An-Najah National University, P.O. Box 7 Nablus, Palestine; [13]MRI Unit, Leibniz Research Centre for Working Environment and Human Factors, Department of Psychology and Neurosciences, Technical University Dortmund, 44139 Dortmund, Germany; [14]Department of Molecular and Clinical Medicine/Wallenberg Laboratory, Sahlgrenska Academy, University of Gothenburg, 41345 Gothenburg, Sweden; [15]University Clinic for Visceral Surgery and Medicine, Inselspital University Hospital, University of Bern, 3010 Bern, Switzerland; [16]Departments of Clinical Pharmacology, and of Biochemistry and Pharmacy, University Tuebingen, 72076 Tuebingen, Germany; [17]Cluster of Excellence iFIT (EXC2180), Image-Guided and Functionally Instructed Tumor Therapies, University of Tuebingen, 69120 Tuebingen, Germany; [18]Institute of Pathology and Department of Nephrology, University Hospital RWTH Aachen, Pauwelsstr. 30, 52074 Aachen, Germany; [19]Department of Nephropathology, Friedrich-Alexander-University Erlangen-Nuremberg, 91054 Erlangen, Germany; [20]Institute of Pathology, Nephropathology Unit, Hannover Medical School, 30625 Hannover, Germany; [21]Department of Pediatrics, Division of Gastroenterology, Hepatology, and Nutrition, Emory University, Atlanta, GA 30322, United States; [22] Division of Gastroenterology and Hepatology, Department of Internal Medicine III, Medical University of Vienna, 1090 Vienna, Austria; [23]Vienna Hepatic Hemodynamic Lab, Division of Gastroenterology and Hepatology, Department of Internal Medicine III, Medical University of Vienna, Vienna, Austria; [24]Hans Popper Laboratory of Molecular Hepatology, Vienna Hepatic Hemodynamic Lab, Division of Gastroenterology and Hepatology, Department of Internal Medicine III, Medical University of Vienna, Vienna, Austria

Abbreviations

AKI, acute kidney injury; AQP, aquaporin; ASBT, apical sodium-dependent bile acid transporter; BAs, bile acids; BDL, bile duct ligation; CN, cholemic nephropathy; KIM-1, kidney injury molecule 1; MALDI-MSI: matrix assisted laser desorption/ionization mass spectrometry imaging; MRP, multidrug resistance-associated protein; NGAL, neutrophil gelatinase-associated lipocalin; TCA, taurocholic acid; TECs, tubular epithelial cells.

Conflict of interest

AG and JGH declare consulting activities for Albireo Pharma. ES and EL are employees of Albireo Pharma. HUM declares consulting or advisory board activities for Albireo Pharma, Calliditas, Intercept, Mirum and Zealand and lecture fees by Albireo, Intercept and Bayer. SJK declares consulting activities for Albireo Pharma, Hemoshear, Intercept Pharma, and Mirum Pharma; PAD has received research grants from Albireo Pharma. B.S. received travel support from AbbVie and Gilead. TR received grant support from Abbvie, Boehringer Ingelheim, Gilead, Intercept/Advanz Pharma, MSD, Myr Pharmaceuticals, Philips Healthcare, Pliant, Siemens and W. L. Gore & Associates; speaking honoraria from Abbvie, Gilead, Intercept/Advanz Pharma, Roche, MSD, W. L. Gore & Associates; consulting/advisory board fee from Abbvie, Astra Zeneca, Bayer, Boehringer Ingelheim, Gilead, Intercept/Advanz Pharma, MSD, Resolution Therapeutics, Siemens; and travel support from Abbvie, Boehringer Ingelheim, Dr. Falk Pharma, Gilead and Roche. M.M. served as a speaker and/or consultant and/or advisory board member for AbbVie, Collective Acumen, Echosens, Gilead, Ipsen, Takeda, and W. L. Gore & Associates and received travel support from AbbVie and Gilead. MT received speaker fees from BMS, Falk Foundation, Gilead, Intercept, Jannsen, Madrigal, and MSD; he advised for Abbvie, Albireo Pharma, BiomX, Boehringer Ingelheim, Falk Pharma GmbH, Genfit, Gilead, Hightide, Intercept, Janssen, MSD, Novartis, Phenex, Pliant, Regulus, Siemens and Shire. He further received travel grants from Abbvie, Falk, Gilead, Intercept and Jannsen and research grants from Albireo Pharma, Alnylam, Cymabay, Falk, Gilead, Intercept, MSD, Takeda and UltraGenyx. He is also co-inventor of patents on the medical use of norUDCA filed by the Medical Universities of Graz and Vienna. MS received travel expenses and research support from Agena Bioscience, CED Service GmbH, and ALL Akademie. MS was involved in clinical trials by Green Cross WellBeing Co.Ltd., Gilead Sciences Inc., CORAT Therapeutics GmbH, Agena Bioscience, and HepaRegenix GmbH.

Please refer to the accompanying ICMJE disclosure forms for further details.

Authors' contributions

AG and JGH: study concept and design, data acquisition, analysis and interpretation of data, manuscript writing, funding, study supervision; DG, MM, RH, ZH, LB, BBT, JR, MV, AS, TA, NA, SAFM, WM, AH, WA, NV, CV, RM, CC, MV, EG, PN, SJK: contributed to study concept and design, data acquisition, manuscript writing, analysis and interpretation of data; ES, PÅ, JM, EL: synthetized AS0369, contributed to study concept and design, data acquisition, manuscript writing, analysis and interpretation of data, funding; UH, MS: bile acid analysis, contributed to manuscript writing, critical revision of the manuscript; JD, CD, FK, JR: bioinformatics analysis, contributed to manuscript writing, critical revision of the manuscript; AF, SH: image analysis, contributed to manuscript writing, critical revision of the manuscript; NK, MA, AS: synthetized fluorescein-coupled TCA, contributed to manuscript writing, critical revision of the manuscript; KE: RNA-sequencing, contributed to bioinformatics analysis, study concept and design, data acquisition, analysis and interpretation of data, critical revision of the manuscript; KA, JS, JHB, PB, BS, TR, MM: clinical data; contributed to study concept and design, analysis and interpretation of data, critical revision of the manuscript; MT, HUM, PAD, GS, TL: contributed to study concept and design, analysis and interpretation of data, critical revision of the manuscript.

Data availability statement

All data presented in this manuscript will be made available to other researchers upon request.

Shivendra Singh, Ramesh Kangarajan, Ashwani Gaur (Syngene International, Bangalore, India) for their contributions to the development of AS0369.

Supplementary data

Supplementary data to this article can be found online at https://doi.org/10.1016/j.jhep.2023.10.035.

References

Author names in bold designate shared co-first authorship.

[1] EASL., EASL. Clinical Practice Guidelines for the management of patients with decompensated cirrhosis. J Hepatol 2018;69:406–460.

[2] Krones E, Pollheimer MJ, Rosenkranz AR, et al. Cholemic nephropathy - historical notes and novel perspectives. Biochim Biophys Acta Mol Basis Dis 2018;1864:1356–1366.

[3] Somagutta MR, Jain MS, Pormento MKL, et al. Bile cast nephropathy: a comprehensive review. Cureus 2022;14:e23606.

[4] Mandorfer M, Aigner E, Cejna M, et al. Austrian consensus on the diagnosis and management of portal hypertension in advanced chronic liver disease (Billroth IV). Wien Klin Wochenschr 2023;135:493–523.

[5] Simbrunner B, Trauner M, Reiberger T, et al. Recent advances in the understanding and management of hepatorenal syndrome. Fac Rev 2021;10:48.

[6] Fickert P, Rosenkranz AR. Cholemic nephropathy reloaded. Semin Liver Dis 2020;40:91–100.

[7] Mandorfer M, Hecking M. The renaissance of cholemic nephropathy: a likely underestimated cause of renal dysfunction in liver disease. Hepatology 2019;69:1858–1860.

[8] **Ariza X**, **Graupera I**, Coll M, et al. Neutrophil gelatinase-associated lipocalin is a biomarker of acute-on-chronic liver failure and prognosis in cirrhosis. J Hepatol 2016;65:57–65.

[9] Arroyo V, Moreau R, Jalan R, et al. Acute-on-chronic liver failure: a new syndrome that will re-classify cirrhosis. J Hepatol 2015;62:S131–S143.

[10] Nayak SL, Kumar M, Bihari C, et al. Bile cast nephropathy in patients with acute kidney injury due to hepatorenal syndrome: a postmortem kidney biopsy study. J Clin Transl Hepatol 2017;5:92–100.

[11] **Fickert P**, **Krones E**, Pollheimer MJ, et al. Bile acids trigger cholemic nephropathy in common bile-duct-ligated mice. Hepatology 2013;58:2056–2069.

[12] Krones E, Eller K, Pollheimer MJ, et al. NorUrsodeoxycholic acid ameliorates cholemic nephropathy in bile duct ligated mice. J Hepatol 2017;67:110–119.

[13] Allegretti AS, Belcher JM. Bile acids are important contributors to AKI associated with liver disease: CON. Kidney360 2022;3:21–24.

[14] Fickert P, Rosenkranz AR. Bile acids are important contributors to AKI associated with liver disease: pro. Kidney360 2022;3:17–20.

[15] Ghallab A, Hassan R, Hofmann U, et al. Interruption of bile acid uptake by hepatocytes after acetaminophen overdose ameliorates hepatotoxicity. J Hepatol 2022;77:71–83.

[16] Ghallab A, Hofmann U, Sezgin S, et al. Bile microinfarcts in cholestasis are initiated by rupture of the apical hepatocyte membrane and cause shunting of bile to sinusoidal blood. Hepatology 2019;69:666–683.

[17] Bábíčková J, Klinkhammer BM, Buhl EM, et al. Regardless of etiology, progressive renal disease causes ultrastructural and functional alterations of peritubular capillaries. Kidney Int 2017;91:70–85.

[18] Wilson FA, Burckhardt G, Murer H, et al. Sodium-coupled taurocholate transport in the proximal convolution of the rat kidney in vivo and in vitro. J Clin Invest 1981;67:1141–1150.

[19] Truong JK, Bennett AL, Klindt C, et al. Ileal bile acid transporter inhibition in Cyp2c70 KO mice ameliorates cholestatic liver injury. J Lipid Res 2022;63:100261.

[20] Kunst RF, de Waart DR, Wolters F, et al. Systemic ASBT inactivation protects against liver damage in obstructive cholestasis in mice. JHEP Rep 2022;4:100573.

Supplemental information

Inhibition of the renal apical sodium dependent bile acid transporter prevents cholemic nephropathy in mice with obstructive cholestasis

Ahmed Ghallab, Daniela González, Ellen Strängberg, Ute Hofmann, Maiju Myllys, Reham Hassan, Zaynab Hobloss, Lisa Brackhagen, Brigitte Begher-Tibbe, Julia C. Duda, Carolin Drenda, Franziska Kappenberg, Joerg Reinders, Adrian Friebel, Mihael Vucur, Monika Turajski, Abdel-latief Seddek, Tahany Abbas, Noha Abdelmageed, Samy A.F. Morad, Walaa Morad, Amira Hamdy, Wiebke Albrecht, Naim Kittana, Mohyeddin Assali, Nachiket Vartak, Christoph van Thriel, Ansam Sous, Patrick Nell, Maria Villar-Fernandez, Cristina Cadenas, Erhan Genc, Rosemarie Marchan, Tom Luedde, Peter Åkerblad, Jan Mattsson, Hanns-Ulrich Marschall, Stefan Hoehme, Guido Stirnimann, Matthias Schwab, Peter Boor, Kerstin Amann, Jessica Schmitz, Jan H. Bräsen, Jörg Rahnenführer, Karolina Edlund, Saul J. Karpen, Benedikt Simbrunner, Thomas Reiberger, Mattias Mandorfer, Michael Trauner, Paul A. Dawson, Erik Lindström, and Jan G. Hengstler

Inhibition of the renal apical sodium dependent bile acid transporter prevents cholemic nephropathy in mice with obstructive cholestasis

Ahmed Ghallab, Daniela González, Ellen Strängberg, Ute Hofmann, Maiju Myllys, Reham Hassan, Zaynab Hobloss, Lisa Brackhagen, Brigitte Begher-Tibbe, Julia Duda, Carolin Drenda, Franziska Kappenberg, Joerg Reinders, Adrian Friebel, Mihael Vucur, Monika Turajski, Abdel-latief Seddek, Tahany Abbas, Noha Abdelmageed, Samy A.F. Morad, Walaa Morad, Amira Hamdy, Wiebke Albrecht, Naim Kittana, Mohyeddin Assali, Nachiket Vartak, Christoph van Thriel, Ansam Sous, Patrick Nell, Maria Villar-Fernandez, Cristina Cadenas, Erhan Genc, Rosemarie Marchan, Tom Luedde, Peter Åkerblad, Jan Mattsson, Hanns-Ulrich Marschall, Stefan Hoehme, Guido Stirnimann, Matthias Schwab, Peter Boor, Kerstin Amann, Jessica Schmitz, Jan H. Bräsen, Jörg Rahnenführer, Karolina Edlund, Saul J. Karpen, Benedikt Simbrunner, Thomas Reiberger, Mattias Mandorfer, Michael Trauner, Paul A. Dawson, Erik Lindström, Jan G. Hengstler

Table of contents

Supplementary methods

Renal biopsies of patients with cholemic nephropathy. A total number of 21 and 11 renal biopsies from CN and non-CN patients, respectively, were collected from two cohorts, the Hannover cohort (14 CN and 4 non-CN biopsies) and the Erlangen cohort (7 CN and 7 non-CN biopsies) (Table S1). The study was conducted according to the ethical guidelines of the 1975 Helsinki Declaration and was approved by the local ethics committee (no. 4415, 22-150-D).

Animals and bile duct ligation. Eight-to-10-week-old male and female C57BL/6N (Janvier Labs, France) or *Cyp2c70*$^{-/-}$ and corresponding C57BL/6J wildtype (Dawson, Karpen Lab) mice were used. The mice were housed at standard environmental conditions with free access to water, and ad libitum feeding with Ssniff R/M-H, 10 mm standard diet (Ssniff, Soest, Germany). All experiments were approved by the local animal welfare committee (LANUV, North Rhine-Westphalia, Germany, application number: 81-02.04.2022.A286). To induce obstructive cholestasis the extrahepatic common bile duct was ligated at a position between the gallbladder and the duodenum, as previously described [1, 2].

Preparation and application of AS0369. A stock formulation was prepared by dissolving AS0369 in the vehicle solution (0.5% methyl cellulose and 0.06% Tween 80) followed by sonication and vortexing for several minutes until a uniform suspension was obtained. The different doses of 15, 30, 60 and 120 mg/kg b.w. were prepared by diluting the stock formulation accordingly in the vehicle solution. The ASBT inhibitor (AS0369) and the vehicle were administered orally by gavage twice per day with an application volume of 4 mL/kg b.w.

Sample collection and processing. Blood sampling. Heart blood samples were collected from anaesthetised mice in syringes precoated with disodium ethylenediaminetetraacetic acid (EDTA), as previously described [3]. After centrifugation, plasma was separated and stored at -80 °C until used for analysis. ***Tissue sample collection.*** Prior to tissue collection, transcardial perfusion with PBS was performed to wash out the remaining blood. *Liver tissue sample collection:* the whole liver was excised.

Samples of 5 × 7 mm diameter were collected from the left liver lobe and fixed for two days in 4% paraformaldehyde (PFA) followed by washing in PBS and embedding in paraffin. In addition, samples of 5 × 7 mm diameter were collected from the left liver lobe, immediately frozen in liquid nitrogen and stored at -80 °C until analysis by MALDI-MSI. The remaining liver tissue was snap-frozen by freeze-clamping and milling in liquid nitrogen, and subsequently stored at -80 °C until RNA isolation. *Kidney tissue sample collection:* both the left and the right kidneys were excised. After removal of the surrounding capsule, the right kidney was divided longitudinally into two halves; one half was fixed in 4% PFA and embedded in paraffin, and the other half was immediately frozen in liquid nitrogen and stored at -80 °C until analysis by MALDI-MSI. The left kidney was snap-frozen by freeze-clamping and milling in liquid nitrogen, and subsequently stored at -80 °C until RNA isolation. **Urine sample collection.** 24-hour urine samples were collected in metabolic cages as previously described [4]. Spontaneous urine samples were collected from female mice using a urinary bladder canula (25 gauge; SAI Infusion Technologies) as previously described [5]. **Bile sample collection.** Bile samples were collected from the gallbladder.

Biochemical analysis. Creatinine, urea, total bilirubin, and direct bilirubin from plasma and/or urine were determined using a C400 clinical chemistry analyzer (Pentra C400 Option I.S.E, HORIBA ABX SAS, Montpellier, France). Biomarkers of liver damage (alanine transaminase, aspartate transaminase and alkaline phosphatase) were measured in mouse plasma using the Piccolo Xpress Chemistry Analyzer (Hitado, Germany) and the Piccolo General Chemistry 13 Panel Kit. The plasma samples from control and BDL mice were diluted 1:1 or 1:5 in normal mouse serum (S7273 -50ML, Sigma-Aldrich), respectively, prior to analysis. AS0369 was analyzed in plasma and tissue samples using LC-MS/MS. **Quantification of bile acids with LC-MS/MS.** Bile acid concentrations in plasma, urine, bile, liver tissue and kidney tissue were determined by negative electrospray (ESI) liquid chromatography tandem mass spectrometry (LC-MS/MS) in multiple-reaction-monitoring (MRM) mode on an Agilent 6495B triple quadrupole mass spectrometer (Agilent, Germany) coupled to an Agilent Infinity II HPLC system as described previously [1]. Briefly, frozen tissue samples were homogenized in methanol: water 1:1 (v/v) in a FastPrep® 24 homogenizer (MP Biomedicals, Santa Ana,

USA) to a final concentration of 40 mg wet tissue/ml as described previously [6]. Aliquots of 5 μL of plasma or diluted bile (1:100), 30 μl of tissue homogenate, or 2 μl of urine were spiked with internal standard solution followed by protein precipitation with methanol and centrifugation. The supernatant was used for LC-MS/MS analysis. Urine samples above the calibration range were diluted with water 1:10 v/v to 1:50 v/v. LC-MS/MS parameters for measurement of bile acids and the internal standards are summarized in Table S2. Protein determination in tissue homogenates was performed with the PierceTM BCA protein assay kit.

ELISA assays: Determination of NGAL concentrations Concentrations of NGAL/Lcn-2 were determined in mouse urine and plasma using the Mouse Lipocalin-2/NGAL DuoSet ELISA kit plus the DuoSet ELISA Ancillary Reagent Kit 2 from R&D systems (DY1857 and DY008) according to the manufacturer's protocol. The concentrations of NGAL/Lcn-2 in human serum were determined using the Human Lipocalin-2/NGAL Quantikine ELISA kit from R&D Systems (DLCN20) following the manufacturer's protocol. The optical density of the color-forming TMB substrate from both assays was measured at 450 nm using a microplate reader (Infinite M200 Pro, Tecan) and the concentration of NGAL/Lcn-2 of each sample was calculated from the standard curve. ***Determination of Kim-1 concentrations.*** Concentrations of Kim-1 were determined in mouse urine and plasma using the Mouse KIM 1 ELISA Kit from Abcam (ab213477) according to the manufacturer's protocol. The concentrations of Kim-1 in human serum were determined using the Human Serum TIM-1/KIM-1 HAVCR Quantikine ELISA kit from R&D Systems (DSKM100). The optical density of the color-forming TMB substrate from both assays was measured at 450 nm using a microplate reader (Infinite M200 Pro, Tecan) and the concentration of KIM-1 of each sample was calculated from the standard curve. ***Determination of cystatin C concentrations.*** Concentrations of Cystatin C were determined in plasma using the Mouse Cystatin C ELISA Kit from Abcam (ab201280) according to manufacturer's protocol. For human serum samples the Human Cystatin C Quantikine ELISA kit from R&D Systems (DSCTC0) was used following the manufacturer's instructions. The optical density of the color forming TMB substrate from both assays was measured at 450 nm using a microplate reader (Infinite M200 Pro,

4

Tecan) and the concentration of Cystatin C of each sample was calculated from the standard curve.

Determination of IC$_{50}$ of AS0369. Mouse IBAT- (10,000 cells) or LBAT- (20,000 cells) overexpressing cells were seeded in 96-well plates in 200 µl MEM-alpha medium supplemented with 10% FBS containing Puromycin (10 µg/ml) and incubated at 37°C in 5% CO_2 for 48 hrs. The incubation medium was decanted from the wells and cells were washed two times with 300 µl of basal MEM-alpha medium (FBS-free). Each time after decanting the medium, plates were tapped against paper towel to ensure maximum removal of residual media. Test inhibitor dilutions (highest test concentration being 10 µM, 3-fold serial dilution, 10 points) prepared in DMSO were added in incubation mix (maintaining 0.2% final DMSO concentration) containing 0.25 µM 3H-Taurocholic acid and 5 µM of cold taurocholic acid. 50 µl of incubation mix containing test inhibitors was then added to the wells (in duplicate) and the plates were incubated for 20 min in a CO_2 incubator at 37°C. After incubation, the reaction was stopped by keeping the plates on ice water mix for 2-3 minutes and then the incubation mix was aspirated completely from the wells. The wells were washed two times with 250 µl of chilled unlabeled 1 mM taurocholic acid dissolved in HEPES-buffered (10 mM) HBSS (pH 7.4). The plates were tapped against a paper towel after every washing step to ensure maximum removal of blocking buffer. 100 µl of MicroScint-20 was added to the wells and kept overnight at room temperature before reading the plates in TopCount NXT™ Microplate Scintillation and Luminescence Counter from PerkinElmer under 3H Test protocol (set at 120 seconds reading time per well).

Histopathology. Hematoxylin and eosin (H&E) and Sirius red staining were performed in 4 µm thick PFA (4%)-fixed paraffin-embedded liver and kidney tissue sections. Hematoxylin staining was performed using the Discovery Ultra Automated Slide Preparation System, as previously described [7]. Eosin staining was performed according to a standard protocol [3]. Sirius red staining was done using a commercially available kit, according to the manufacturer's instructions. To visualize bilirubin casts in kidney tissues, Hall's staining was performed using 4 µm-thick PFA (4%)-fixed paraffin-embedded kidney tissue sections using a commercially available kit (StatLab), according to the

manufacturer's instructions. The principle of this staining technique is that oxidation of bilirubin in acidic medium results in formation of biliverdin which can be distinguished by its green color [8]; the cell cytoplasm stains yellow, while collagen appears red.

Immunohistochemistry. Immunostainings were performed using 4 µm-thick PFA (4%)-fixed paraffin-embedded liver and/or kidney tissue sections using the Discovery Ultra Automated Slide Preparation System, as previously described [9, 10]. Antibodies and their concentrations are given in Table S3. Nuclei were visualized by counter-staining with Mayer's hematoxylin. Whole slide scanning was performed using the Axio Scan.Z1.

Image analysis. High-resolution whole slide scans (~1 Gpixel each) were preprocessed using CLAHE, a widely used image processing technique improving the contrast in images by stretching the intensity distribution of the pixels [11] implemented in the software TiQuant [12]. The resulting data was segmented in a two-step process, starting with a Random Forest classification [13] to distinguish tissue and non-tissue regions, and a region of interest within the tissue typically emphasized by staining. Random forest classification is an accurate and robust machine learning technique, whereby features are chosen based on the highest information gain. The model to classify each pixel was manually trained by a subset of images for each staining but was applied to all images using the software QuPath [14]. In a second segmentation step, we refined the segmentation result using the TiQuant software by a semantically informed application of morphological operators that considered known structure shape, size, and localization in tissue to further improve the segmentation accuracy. The diameter of the bile canaliculi network was measured using a pruned skeletonization of the bile network segmentation by averaging the diameter of the maximally inscribed spheres along the skeleton[15].

Intravital imaging. Functional intravital imaging of livers and kidneys of anesthetised mice was performed using an inverted two-photon microscope LSM MP7 or LSM880 (Zeiss, Germany), as previously described [9, 16-18]. Before recording, the mice received bolus tail vein injections of Hoechst 33258 (nuclear marker), TMRE (mitochondrial membrane potential marker), SYTOX green (cell death marker), 2',7'dichlorofluorescein diacetate (H_2DCFDA; a non-fluorescent probe that passes passively into cells, de-esterified intracellularly, and turns to the green-fluorescent dichlorofluorescein (DCF) upon oxidation) and/or anti-CD31 antibody (endothelial cell marker) (Table S4). To allow

administration of further functional dyes/markers while recording, a mouse catheter (SAI-infusion, IL, USA) was fixed in the tail vein. To analyse bile flux in the liver and kidneys, fluorescently labelled taurocholic acid (TCA) or the bile acid analogue CLF was administered via the tail vein catheter as a bolus (Table S4) [9]. To check the integrity of peritubular capillaries, a bolus of the leakiness marker Evans blue [19] was administered and intravital recording was done using the LSM880 confocal microscope (Table S4). At least three mice were analysed for each of the experimental scenarios shown in the result section.

Video analysis. As preprocessing for quantification of intravital imaging, rigid-body registration was performed using StackReg [20] to compensate for tissue motion (e.g., due to respiration and heartbeat) in the time series. Two-dimensional projections were created from these stabilized videos by z-projection using the average, maximum, and standard deviation operators. The autocontext segmentation workflow of the ilastik interactive image segmentation software (version 1.3.3post1) [20] was used to segment the tissue compartments in these 2D projections. The analyzed compartments were peritubular capillaries and TMRE positive tubular epithelial cells in the kidney time series showing TCA uptake, and capillaries and interstitium in the time series visualizing Evans blue dynamics. In the liver, the considered compartments were sinusoidal capillaries, hepatocytes, and bile canaliculi showing TCA flux. Mean raw TCA / Evans blue intensities were measured per compartment and frame. Additionally, the mean TCA signal in the TMRE positive cell compartment was measured per tubule, and tubules were subsequently separated into two groups based on their maximum mean TCA intensity over time using k-means clustering.

Synthesis of TCA-FITC

TCA-FITC was synthetized according to the following scheme:
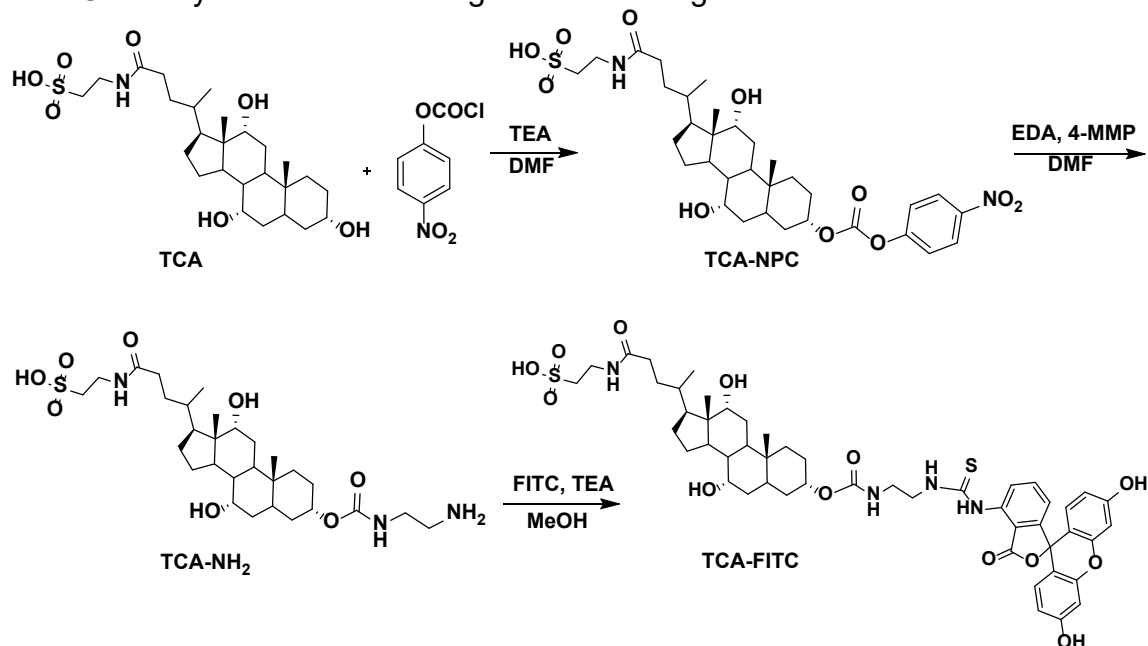
Synthesis of TCA-NPC. A mixture of taurocholic acid (250 mg, 0.465 mmol), 4-nitrophenyl chloroformate (4-NPC) (465 mg, 2.31 mmol), and triethylamine (TEA) (0.5 ml) in DMF (2.5 ml) was stirred at 0 °C for one hour under argon and then, the reaction was left at room temperature for the next day. The crude product was purified by the addition of ethyl acetate (30 ml) in an ice bath to obtain yellowish precipitation separated by centrifugation for 10 mins at 4000 rpm. The precipitate was washed three times with ethyl acetate and then dried under vacuum. The obtained product was dissolved in water and then lyophilized to obtain a white powder with a yield of 90%. ***Synthesis of TCA-NH₂.*** To a solution of TCA-NPC (325 mg, 0.48 mmol) in DMF (4 ml), 4-methyl morpholine (4-MMP) (0.11 ml, 0.96 mmol) was added at 50 °C and left stirred for one hour. Then, ethylenediamine (EDA) (3.22 ml, 48.1 mmol) was added dropwise at room temperature for 30 mins and the reaction was left for the next day. The reaction was evaporated, and acetonitrile was added to remove the unreacted 4-MMP and EDA and the product was precipitated and filtrated. The precipitated product was redissolved in 1M DMF and recrystallized by the addition of ethyl acetate and dried under vacuum. The yield was 92%

with an R$_f$ = 0.25 (DCM:MeOH 5:1) stained by ninhydrin. **Synthesis of TCA-FITC.** A solution of TCA-NH2 (50 mg, 0.05 mmol) in anhydrous methanol (1.5 ml) was added to a solution of FITC (29 mg, 0.075 mmol), TEA (0.2 ml) in anhydrous methanol (2.5 ml) under argon and stirred at 45 °C for 24 hours. After that, the reaction was evaporated and purified by column chromatography with a mobile phase DCM: MeOH (5:1) with a yield of 60%. The ^{1}H NMR spectrum confirms the successful synthesis of the TCA-FITC as in the
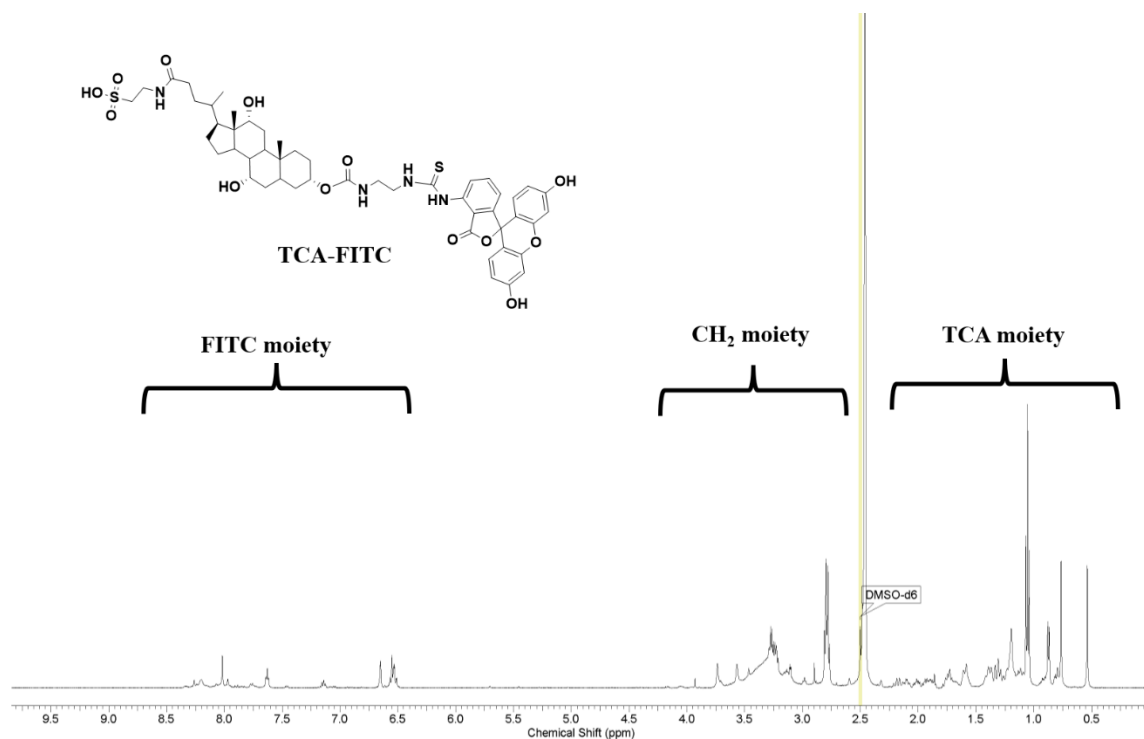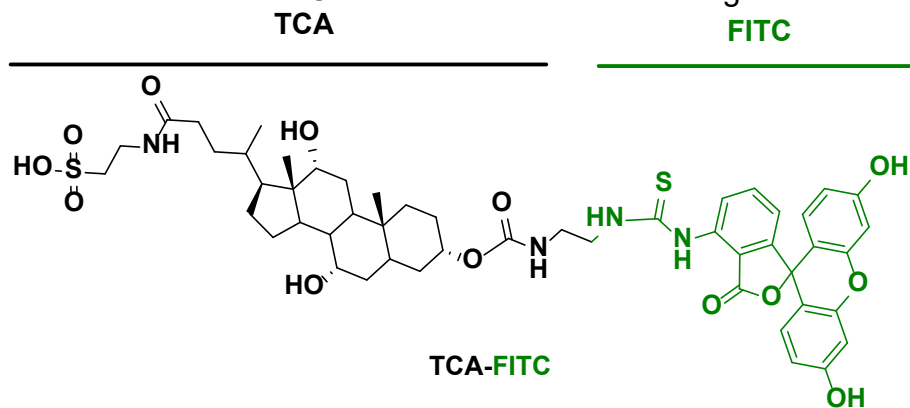

figure below:

The chemical structure of the FITC-labelled taurocholic acid is given in the figure below:

TCA-FITC

MALDI-MS-Imaging. Frozen specimens were sectioned serially into 5-µm-thick tissue sections using a Leica CM 3050 S cryostat. The sections were thaw-mounted on IntelliSlides (Bruker Daltonics, Bremen, Germany), dried in a desiccator, and stored at -20 °C until analysis. The tissue sections were sprayed (4 layers) with 5 mg/mL 2-mercaptobenzothiazole in acetone/water (5:1) using an HTX Imaging-Sprayer (HTX Technologies LLC, Chapel Hill, NC, USA) at 65 °C at 10 psi nitrogen. The flow was 120 µL/min. MALDI-measurements were accomplished on MS1-level in negative mode with a tims TOF FleX without ion-mobility separation in a mass range from 85-800 m/z and calibrated internally using the 2-mercaptobenzothiazole matrix peak and taurocholate. Data was interpreted using Scils Lab MVS, Version 2021 c.

Gene expression analysis

RNA isolation and cDNA synthesis. Liver and kidney RNA was isolated from milled frozen tissue using the RNeasy Mini Kit, according to the manufacturer's protocol. cDNA synthesis was performed from 2 µg of isolated RNA using the High-Capacity cDNA Reverse Transcription Kit. **qRT-PCR assays.** qRT-PCR analyses were performed with cDNA using TaqMan 7500 Real-Time PCR, TaqMan universal PCR Master Mix, and

TaqMan gene expression assays (Table S5) (ThermoFisher Scientifics, Oberhausen, Germany). The gene expression values were normalized to the housekeeping gene GAPDH and further calculated with the $\Delta\Delta$Ct method. The values were expressed as fold changes over control samples.

RNA-sequencing and bioinformatics. RNA-seq of liver and kidney tissues was performed as previously described [21]. Transcript quantification of RNA-seq data and mapping of the FASTQ files were performed with the software Salmon, version 1.4.1, using the option 'partial alignment' and the online provided decoy-aware index for the mouse genome [22]. Further analyses were performed with R, version 4.2.2 [23]. To summarize the transcript reads on gene level, the R package tximeta was used [24]. For pre-filtering, genes with less than 10 reads across all mice (18,872) were removed, so that 16,855 genes remained for further analyses. The following analyses were performed separately for kidney and liver samples. Differential gene expression analysis was calculated using the R package DESeq2 [25]. A general linear model with one factor and levels "sham vehicle", "BDL vehicle" and "AS0369 BDL" was fitted to calculate differentially expressed genes (DEGs). DEGs were then calculated for the comparisons "sham vehicle vs. BDL vehicle" and "sham vehicle vs AS0369 BDL". For more reliable effect estimates, adaptive shrinkage was applied [26]. This leads to shrinkage of log-2 transformed fold-changes ($\log_2$(FCs)) towards zero if expression changes are mostly due to noise, whereas relevant $\log_2$(FCs) are preserved. For each comparison, a gene was considered to be differentially expressed if the effect size fulfils $\log_2$(FC) > $\log_2$(1.5) for upregulation ($\log_2$(FC) < -$\log_2$(1.5) for downregulation) and the estimate is significantly different from zero (i.e., no effect) with a false discovery rate (FDR)-adjusted p-value p_{adj} < 0.05. DiPa (Nell) plots were generated as recently described [27]. Enrichment analysis for biological processes gene ontology (GO) terms was applied separately for up and down regulated genes for the above described comparison "sham vehicle vs. BDL vehicle" and two of the areas defined in the differentiation pattern (DiPa) plot (Fig 7C, I) using the R package topGO [28]. P-values of GO groups were FDR-adjusted and considered significant if the adjusted p-value was smaller than 0.05. To compare DEGs between liver and kidney, Venn diagrams were used, and the corresponding overlap ratios were calculated as previously described [29]. The overlap ratio between two sets

of genes indicates the degree of overrepresentation in the overlap of the two gene sets compared to a random situation. If the ratio is higher than 1, the number of genes in the overlap is higher than randomly expected. The overlap ratio is calculated as follows: If $n_{universe}$ is the total number of analyzed genes, n_1 and n_2 are the numbers of DEGs in gene set 1 and 2, and O is the number of genes present in both sets, then: Overlap ratio = ($O \cdot n_{universe}$) / ($n_1 \cdot n_2$).

Statistical analysis. Mouse data. Data were analyzed using Prism software (GraphPad Prism 9.5.0 Software, Inc., La Jolla, CA, USA). Statistical group comparisons were done using Tukey's, Dunn's, or Šídák's multiple comparisons test, or unpaired t-test, as indicated in the figure legends. Statistical analysis of genome-wide gene expression was done using R (version 4.2.2) [23]. **Serum data of liver disease patients and healthy volunteers.** Correlation between sum bile acids, total bilirubin, and KIM-1 in serum was calculated by the Spearman correlation test. In the multiple linear regression analysis (stepwise backward selection) KIM-1 (pg/mL) was the dependent variable, while sum bile acids (µmol/L), total bilirubin (mg/dL), C-reactive protein (mg/dL), and UDCA therapy (yes, no) were tested as covariables. Mean arterial pressure (mmHg) was not analysed as a covariable, because only three patients showed values smaller than 70 mmHg. Differences in serum values between patients and controls were tested by the two-sided Wilcoxon test for unpaired data. The analyses were performed with SPSS version 29.

Supplementary video legends

Video S1: Reduced uptake of bile acids at the blood side of hepatocytes after bile duct ligation. A. Control mouse; **B.** Bile duct-ligated mouse (day 21). The time in the left corners indicates the minutes after TCA injection into the tail vein. Red: TMRE; green: TCA; blue: Hoechst. The videos correspond to Suppl. Fig. 2

Video S2: Zonated enrichment of TCA in renal tubular epithelial cells after bile duct ligation. A. Sham control mouse; **B.** Bile duct-ligated mouse (day 21) showing zonated enrichment of TCA in renal tubular epithelial cells (asterisk). The time in the left corners indicates the minutes after TCA injection into the tail vein. Red: TMRE; green: TCA; blue: Hoechst. The Videos correspond to Fig. 1A, B of the main manuscript.

Video S3: Time-resolved events after BDL. A. Intravital imaging of cell death (SYTOX green positive) of proximal tubular epithelial cells, release of cell debris into tubular lumen (example in the yellow circle) and cast formation in the distal tubules (white circles) and collecting ducts (blue circles). The proximal tubules are indicated by higher intensity of the mitochondrial potential marker TMRE. Green: SYTOX green; blue: Hoechst; red: TMRE. The video corresponds to Fig. 2C of the main manuscript. **B.** Intravital imaging of glomerular filtration of CLF (white circles) and leakage in the interstitial tissue of a 9-week BDL mouse. Note the dilatation of the Bowman's capsule after glomerular filtration of CLF (circles). Red: TMRE; green: CLF; blue: Hoechst. The video corresponds to Fig. 2B of the main manuscript.

Video S4: Renal peritubular capillary leakiness after BDL. Intravital imaging of Evans blue in 6-week sham-operated (A) or BDL (B) mice. Minutes after tail vein injection of Evans blue are given in the left corners. The videos show leakage of Evans blue into the interstitial tissue (asterisk) in the BDL but not in the sham-operated mouse. Magenta: Evans blue; blue: CD31 (endothelial cell marker). The videos correspond to Fig. 2E, F of the main manuscript.

Video S5: ASBT inhibition prevents the leakiness of renal capillaries after BDL. Intravital videos of mice after tail vein injection of Evans blue. **A.** sham + vehicle; **B.** A BDL mouse treated with vehicle showing leakage of Evans blue into the interstitial tissue (asterisk) within minutes after tail vein injection; **C.** BDL + AS0369. Magenta: Evans blue; blue: CD31. The videos correspond to Fig. 6D-G of the main manuscript.

Supplementary figures
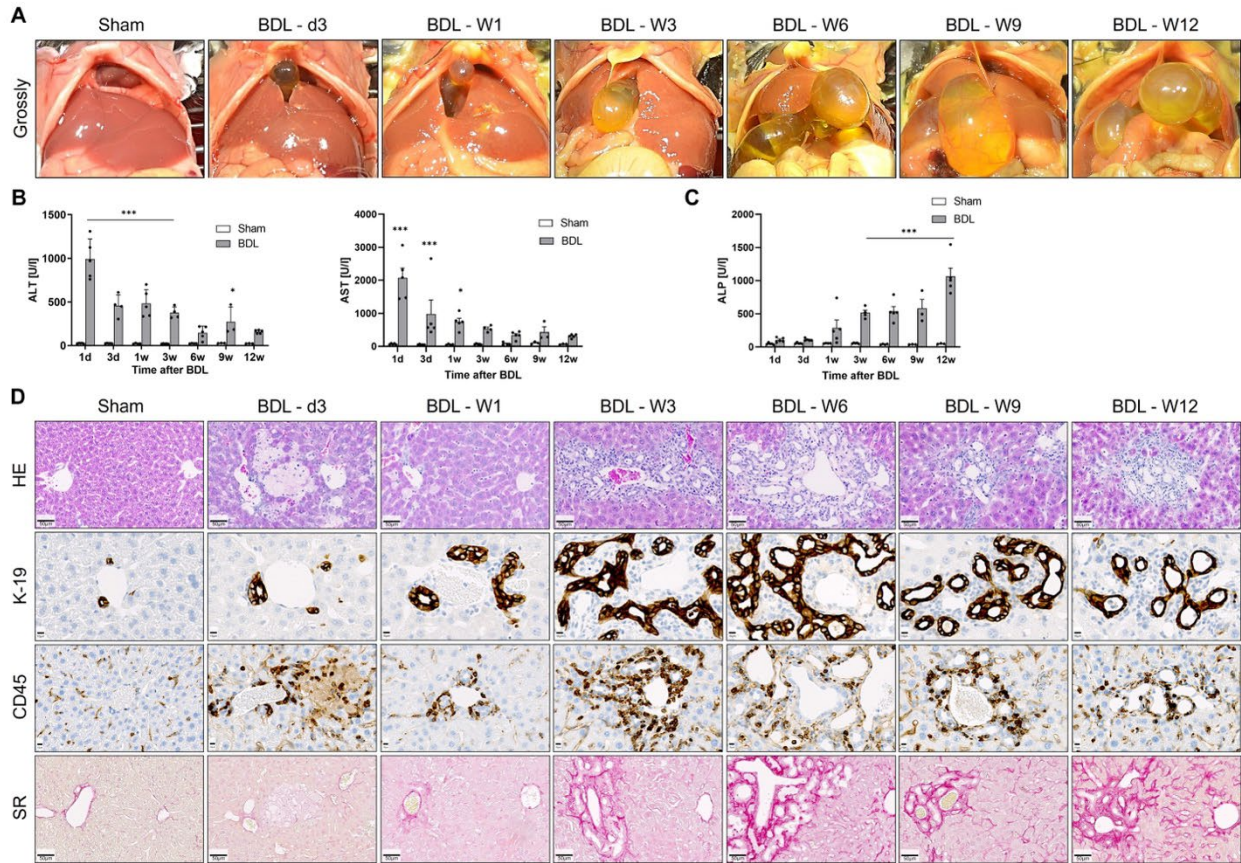
Fig. S1: Clinical chemistry and histology of the liver after BDL. A. Gross pathology. **B.** Plasma activities of ALT and AST. **C.** ALP activity. *p< 0.05; **p< 0.01; ***p< 0.001 compared to the corresponding sham controls, Šídák's multiple comparisons test. **D.** Histological analysis by hematoxylin and eosin (HE) staining (Scale bars: 50 μm), analysis for ductular reaction by the cholangiocyte marker K-19, immune cell infiltration by the pan-leukocyte marker CD45 (scale bars: 10 μm), and fibrosis as evidenced by Sirius red staining; scale bars: 50 μm.
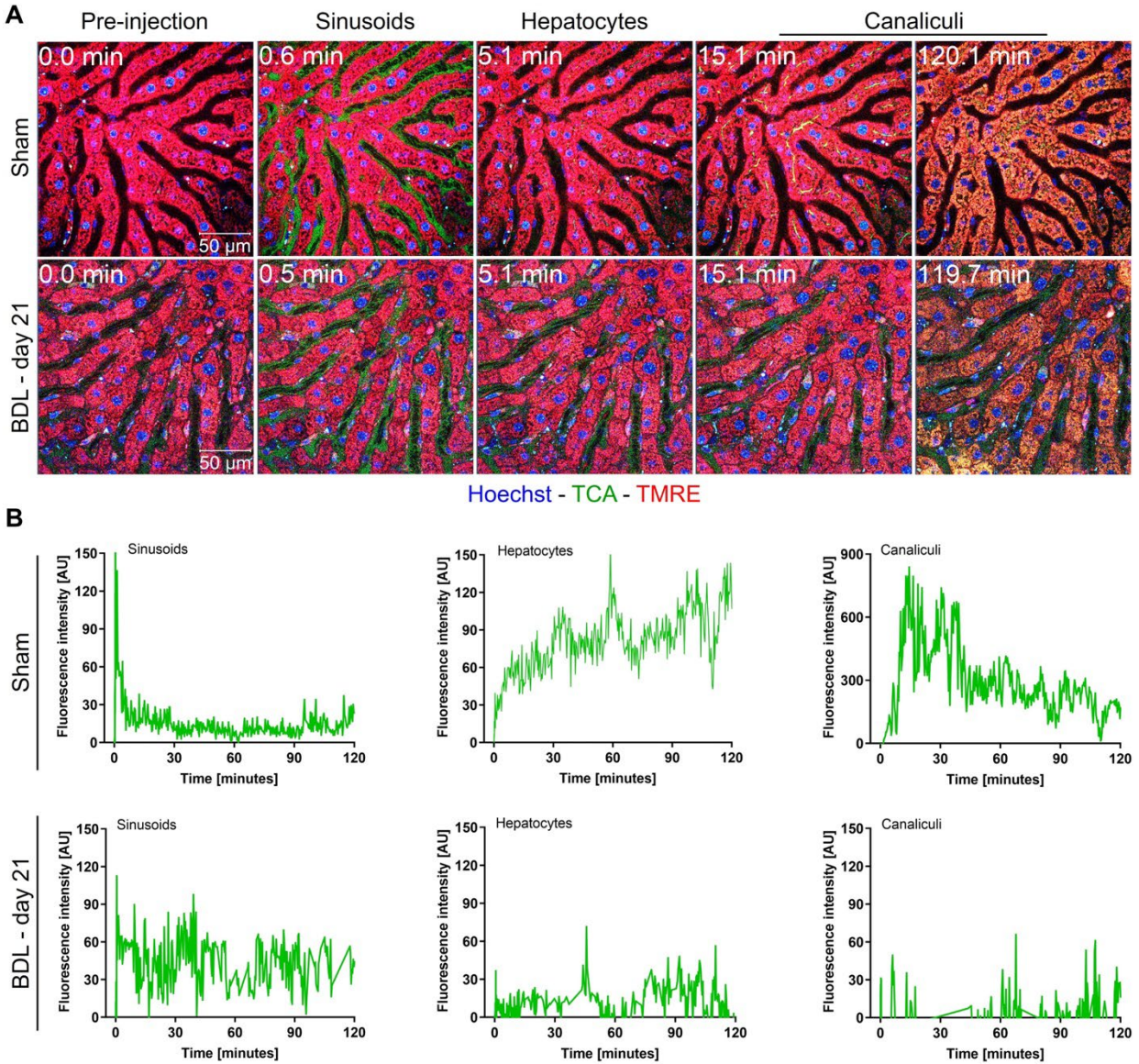
Fig. S2: Reduced uptake of bile acids at the blood side of hepatocytes after BDL. A. Stills from intravital videos in control mice (sham) and 21 days after BDL. The time indicates minutes after tail vein injection of fluorophore coupled TCA; scale bars: 50 µm; Red: TMRE; green: TCA; blue: Hoechst. The stills correspond to Suppl. Videos 1A and 1B. **B.** Quantification of the TCA signal in the blood sinusoids, hepatocytes, and bile canaliculi of the sham (upper panel) and the BDL (lower panel) mice.
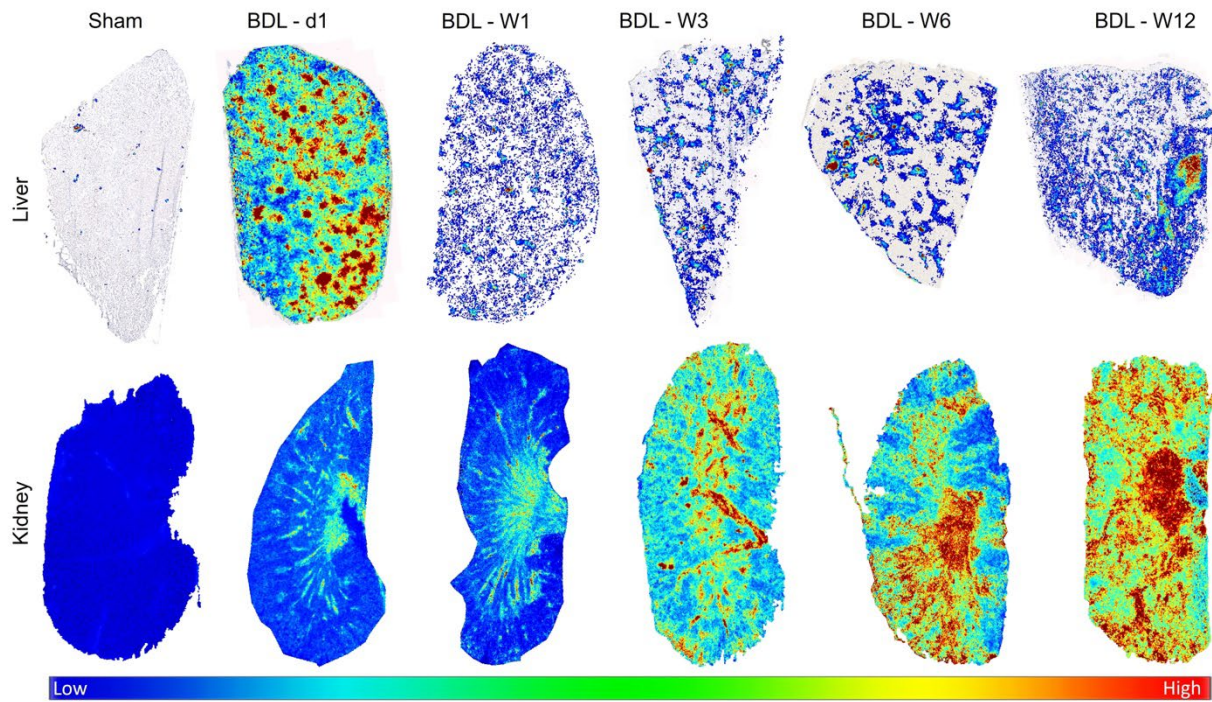
Fig. S3: Transient versus progressive enrichment of TCA in liver and kidney, respectively, after BDL. Cryosections of whole organ sections were analyzed by MALDI-MSI and the TCA signal was superimposed onto K-19 (liver, upper panel) or H&E (kidney, lower panel) staining. The corresponding quantifications are given in Fig. 1F of the main manuscript.
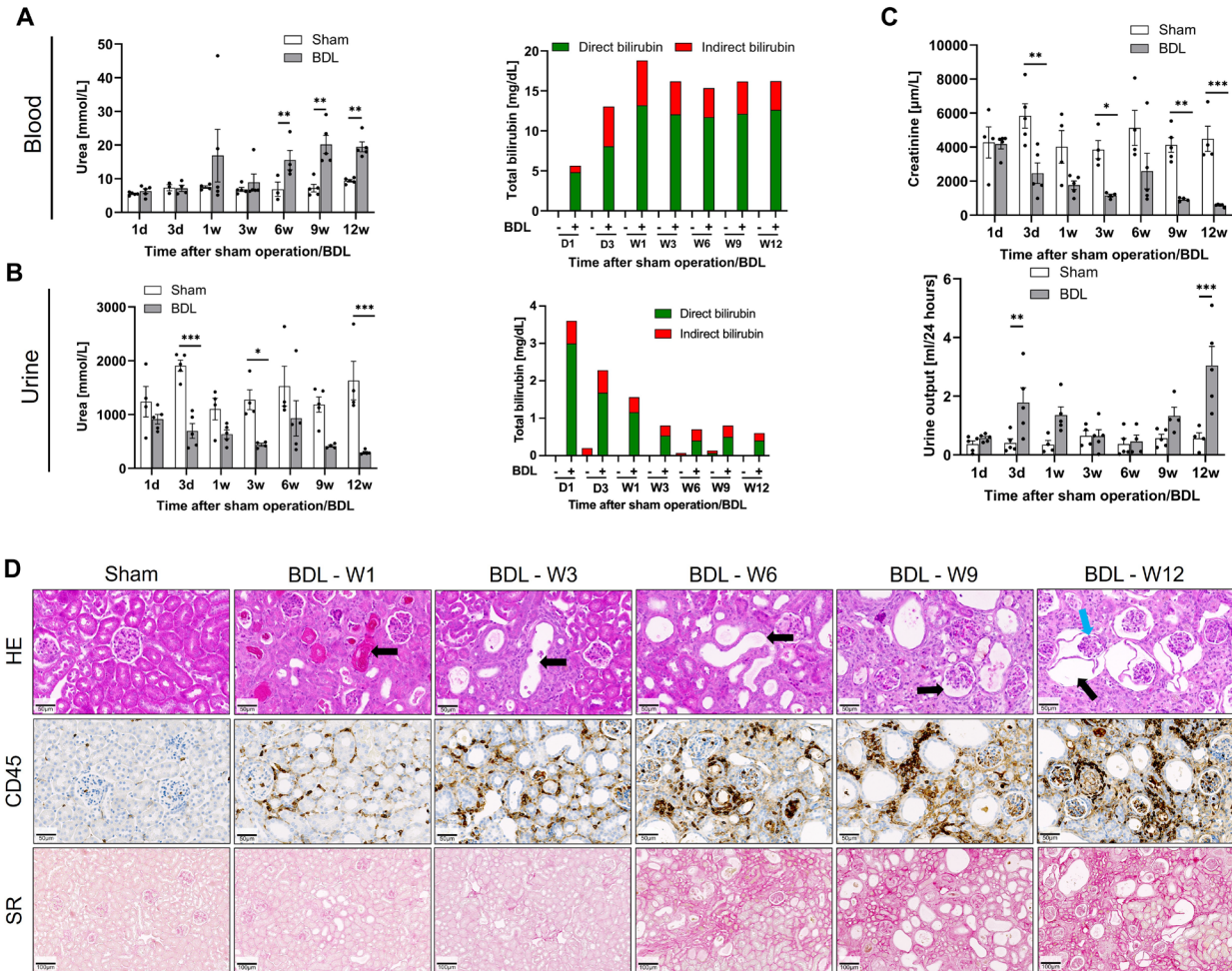
Fig. S4: A, B. Biomarkers of kidney injury in blood and in urine, and urine output; data are presented as means ± SEM; n= 5 mice per group. *p< 0.05; **p< 0.01; ***p< 0.001 compared to the corresponding sham controls, Šídák's multiple comparisons test. . **D.** Histology of the kidney after BDL. The images show the gross pathology; HE staining with cast formation (arrow on week 1), cystic dilatation of renal tubules (arrows at weeks 3 and 6), and glomerular cysts (arrows at weeks 9 and 12; the blue arrow at week 12 indicates atrophy of glomerular capillaries); the pan-leukocyte marker CD45 (scale bars: 50 μm); Hall's stain to visualize 'bile casts' in green (arrow; scale bars: 50 μm); and fibrosis based on Sirius red staining (scale bars: 100 μm).
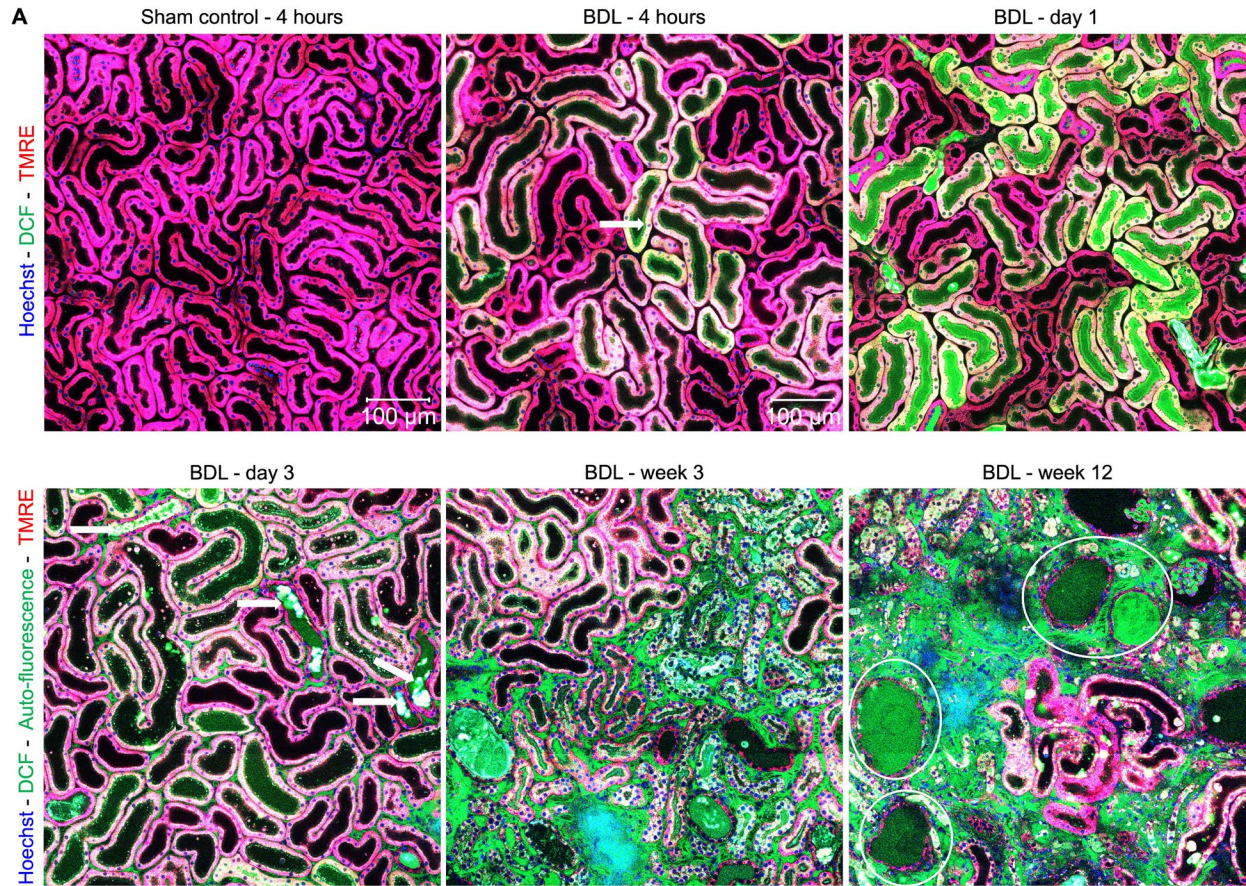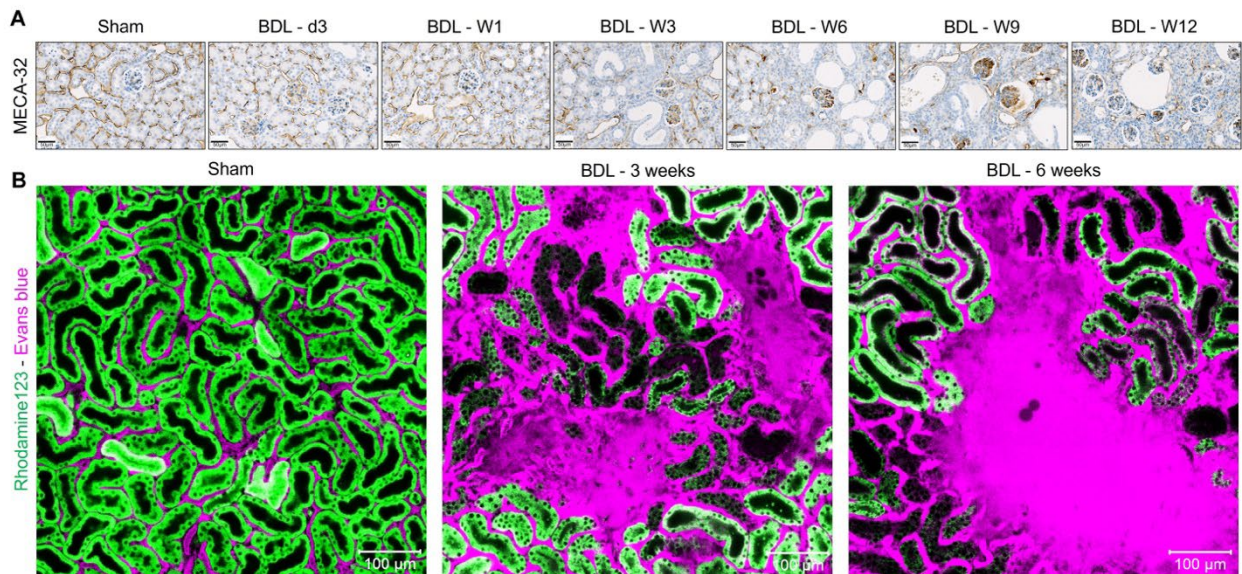
Fig. S5A: Sequence of events in the pathogenesis of cholemic nephropathy. Overview images of the kidneys at different time intervals after BDL showing the following sequence of events: (1) zonated oxidative stress in the proximal tubular epithelial cells (BDL 4 hours, arrow – day 1), (2) cell death of proximal tubular epithelial cells (days 1-3), (3) cast formation in distal tubules (day 3, arrows), (4) peritubular capillary leakiness (weeks 3 and 12), and (5) glomerular cysts (week 12, circles). Red: TMRE (the proximal TEC can be differentiated from distal tubules by their higher TMRE intensity); green: DCF (oxidative stress marker); blue: Hoechst; scale bars: 100 µm. The images correspond to Fig. 2B of the main manuscript.

B

Sham control   BDL - day 1

Hoechst - SYTOX Green - TMRE
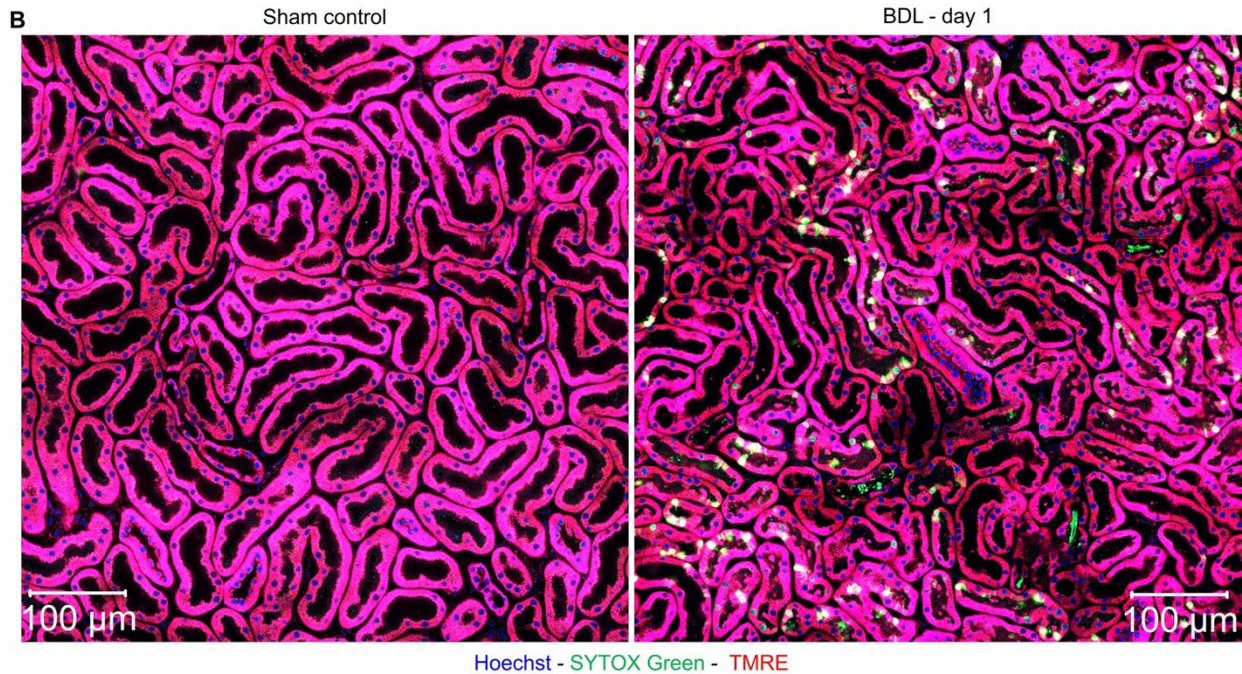
Fig. S5B: Zonation of cell death in proximal tubular epithelial cells on day 1 after BDL. The proximal tubular epithelial cells differ from the distal tubular epithelial cells by the higher intensity of the mitochondrial potential marker TMRE. Red: TMRE; green: SYTOX green (cell death marker); blue: Hoechst; scale bars: 100 µm. The images correspond to Fig. 2C of the main manuscript.

A

MECA-32

Sham   BDL - d3   BDL - W1   BDL - W3   BDL - W6   BDL - W9   BDL - W12

B

Rhodamine123 - Evans blue

Sham   BDL - 3 weeks   BDL - 6 weeks

Fig. S6: Endothelial damage and leakiness of peritubular capillaries after BDL. A. Immunostaining with antibodies directed against the endothelial cell antigen MEC-32; scale bars: 50 µm. **B.** Intravital imaging after tail vein injection of Evans blue in control mice and 3 as well 6 weeks after BDL. Magenta: Evans blue; green: rhodamine123; scale bars: 100 µm.
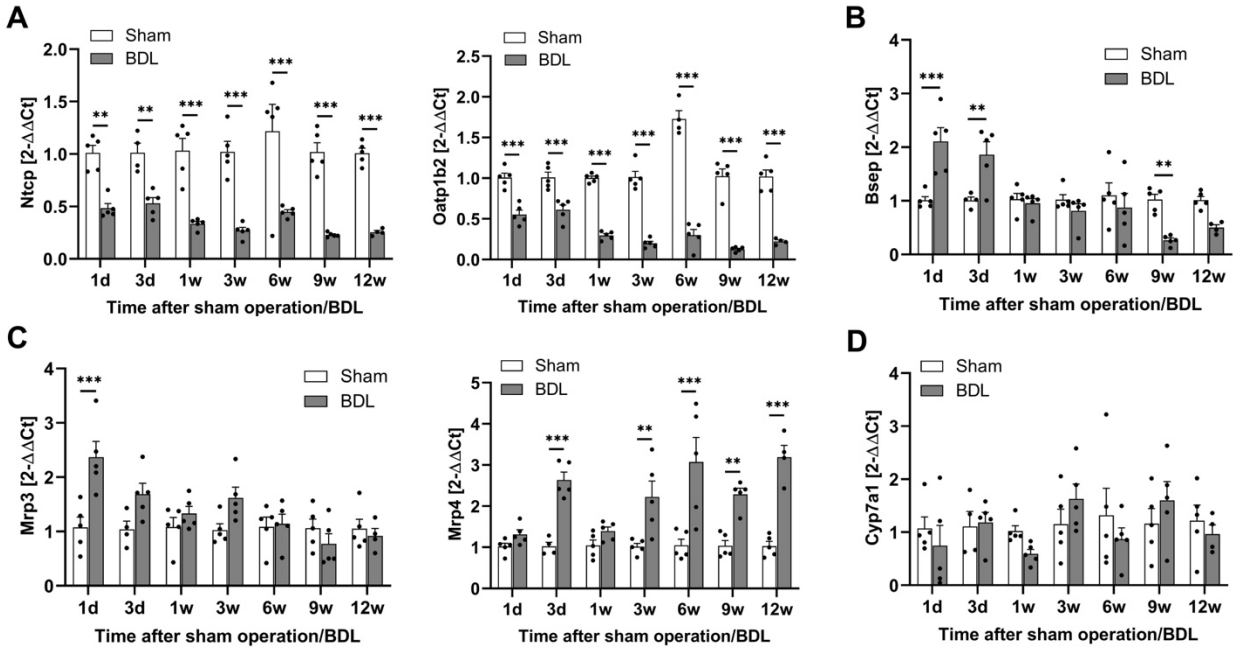
Fig. S7: Expression of bile acid transporters (A-C) and *Cyp7a1* (D) in the liver at different time intervals after BDL. **p< 0.01; ***p< 0.001 compared to the corresponding sham controls; Šídák's multiple comparisons test.
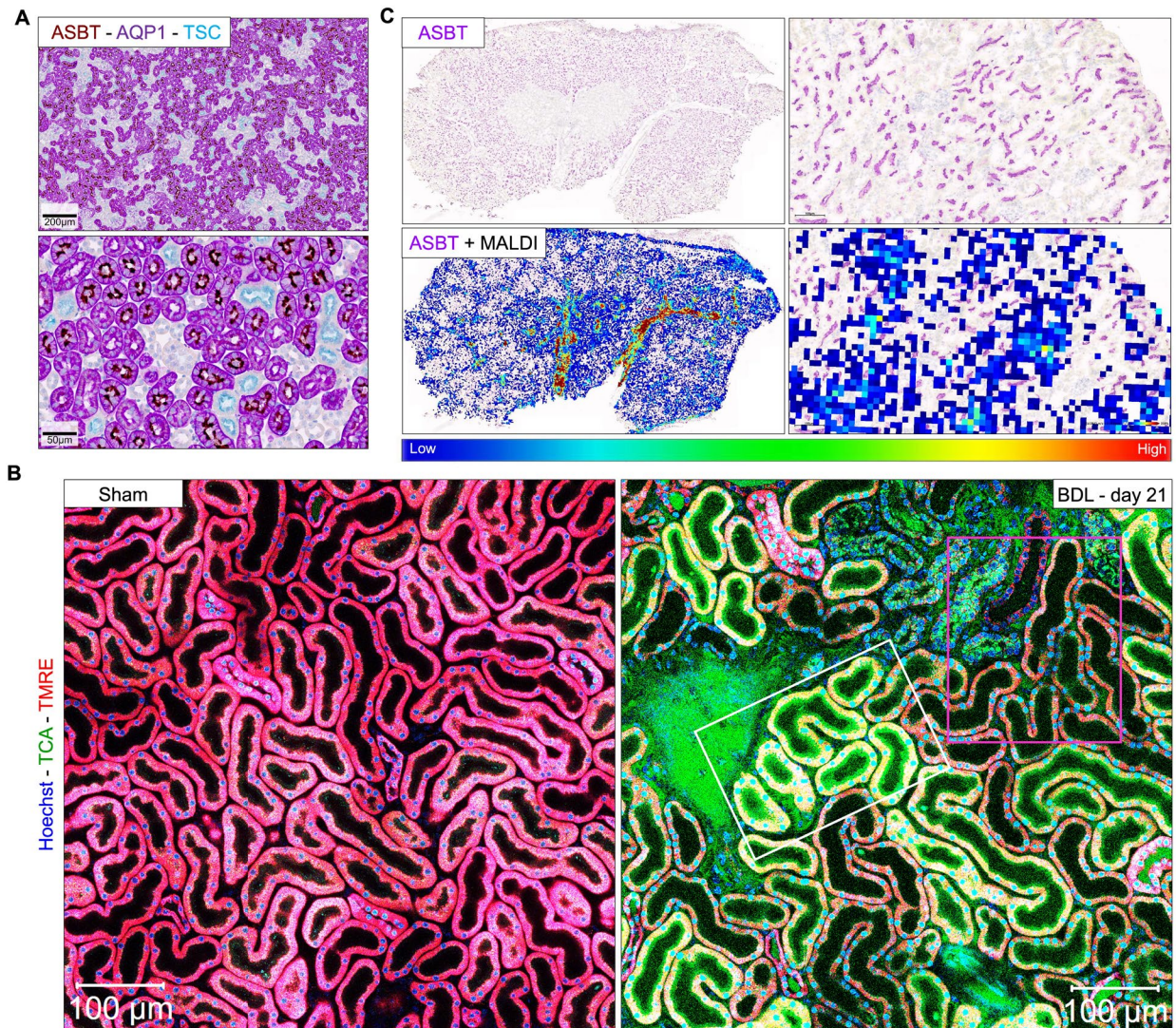
**Fig. S8: Zonated expression of ASBT and bile acid uptake in renal tubular epithelial cells.**
A. Co-immunostaining of ASBT together with the proximal tubule marker AQP1 and the distal tubule marker TSC in renal tissue of control mice. **B.** Intravital imaging of fluorophore coupled TCA in the kidneys of control mice and of mice three weeks after BDL showing zonated enrichment of TCA in proximal (white rectangle) but not the distal (pink rectangle) tubular epithelial cells after BDL. **C.** MALDI-MSI imaging of TCA superimposed onto ASBT immunostaining in kidney tissue of a BDL mouse (day 1) showing zonated enrichment of TCA in regions with ASBT positive renal tubular epithelial cells.
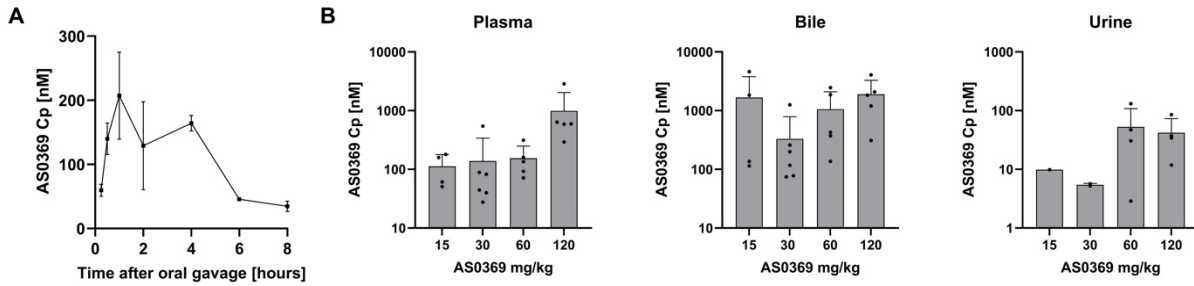
Fig. S9: A. Pharmacokinetics of AS0369 in wild-type mice after oral administration of 10 mg/kg. **B.** Plasma, bile and urinary concentrations of AS0369 in BDL mice after repeated twice daily oral application of various doses for 5 days; the analysis was done 4-7 hours after administration of the last dose of AS0369.
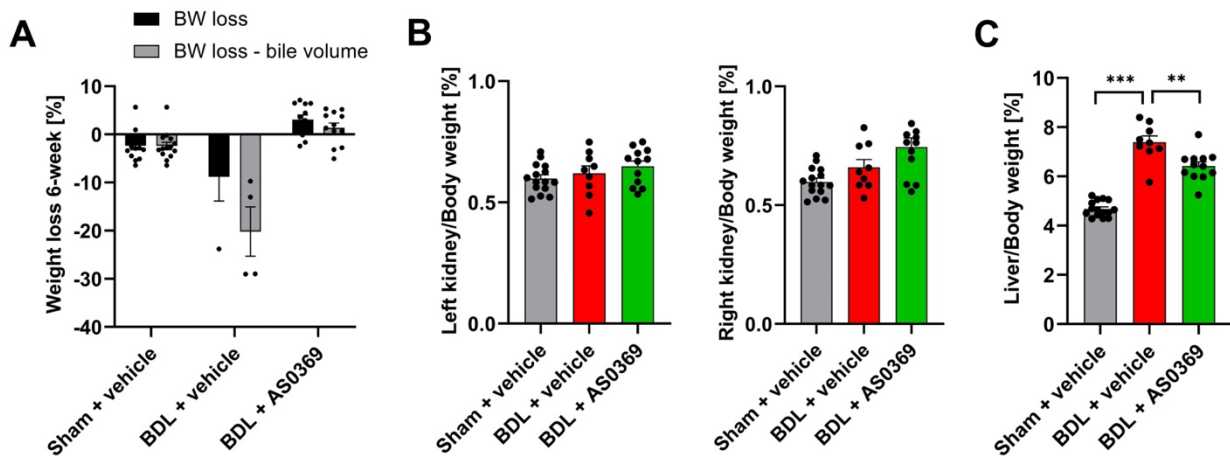
Fig. S10: A. Body weight of mice with BDL after administration of AS0369 or the vehicle, and sham operated mice with vehicle, with and without exclusion of the bile volume. **B, C.** Liver-to-body weight and kidney-to-body weight changes of mice with BDL after administration of AS0369 or the vehicle and sham operated mice with vehicle. **p< 0.01; ***p< 0.001 compared to the corresponding sham controls, Tukey's multiple comparisons test.
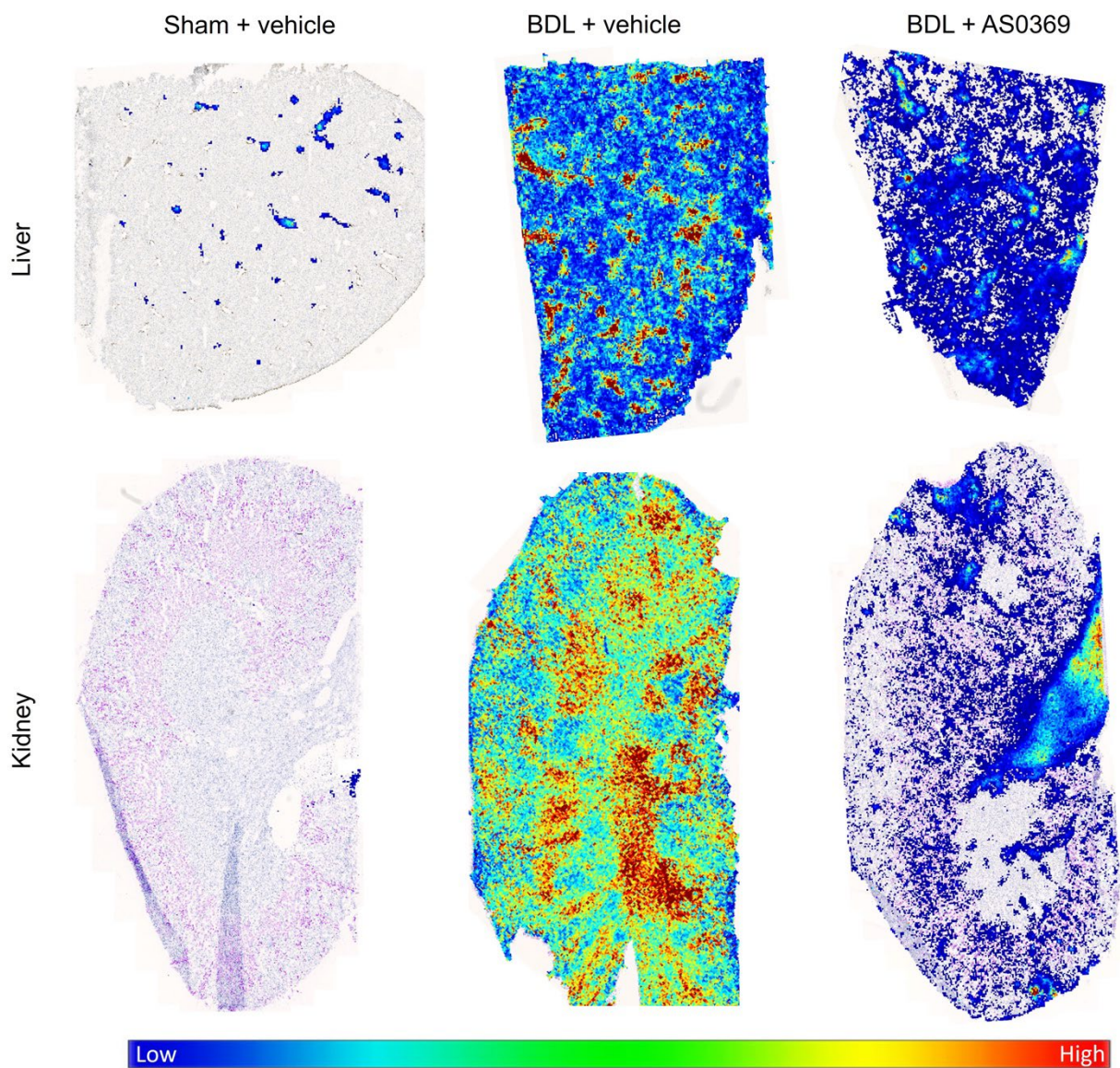
Fig. S11: ASBT inhibition reduces accumulation of bile acids in liver and kidney tissues after BDL. MALDI-MSI analysis of TCA was performed in mice of the three treatment groups illustrated in Fig 5A of the main manuscript. The upper panel shows the MALDI signal of TCA superimposed onto K-19 staining of liver tissue cryosections. The lower panel shows the MALDI signal of TCA superimposed onto ASBT staining of kidney tissue cryosections. The corresponding quantifications are given in Fig. 5H of the main manuscript.
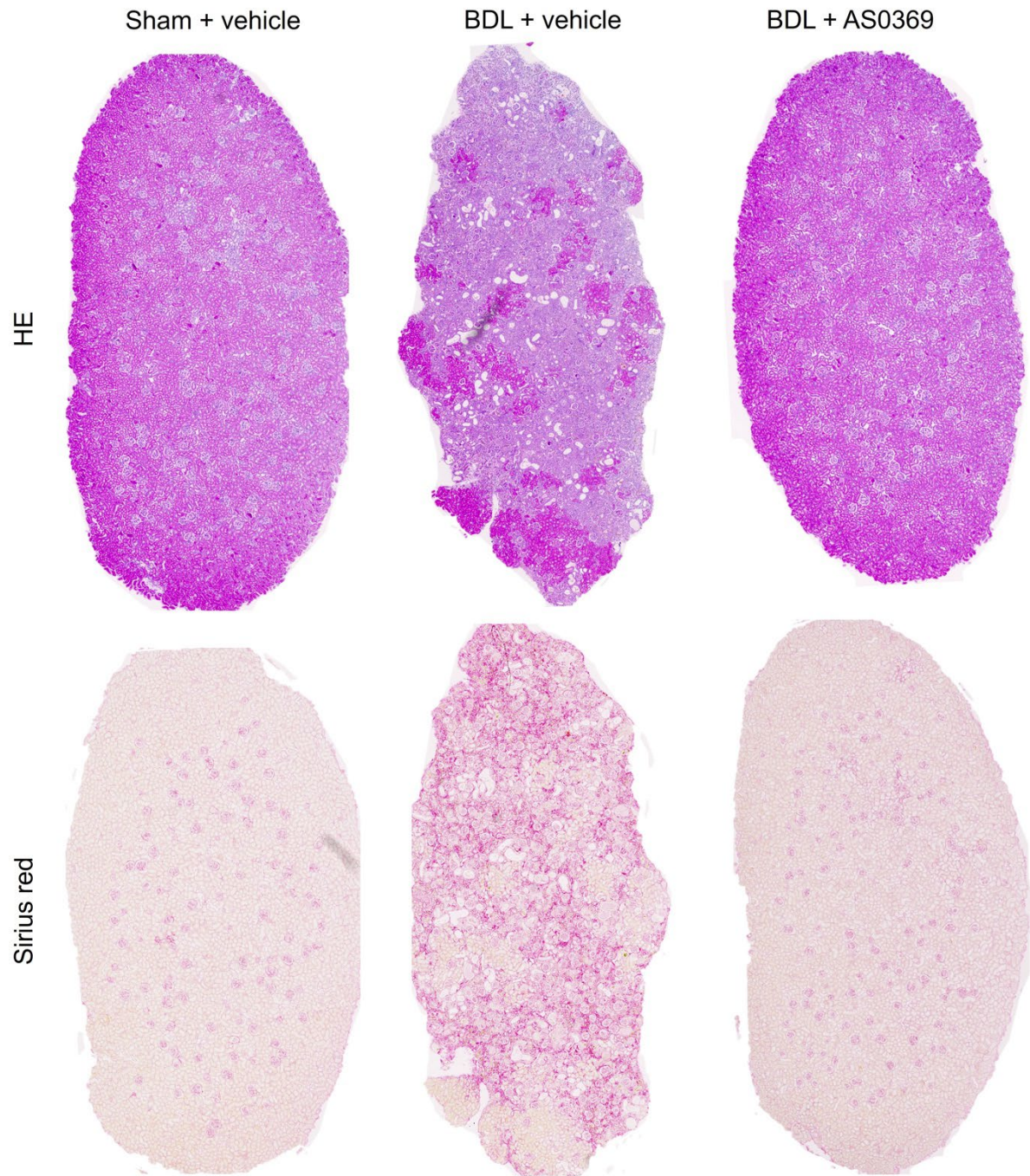
Fig. S12: ASBT inhibition prevents renal tubular epithelial cell damage and fibrosis. Whole organ sections of the kidney of mice according to the treatment schedule of Fig 5A stained with H&E (upper panel) and Sirius red (lower panel). The corresponding quantifications are given in Fig. 6B of the main manuscript.
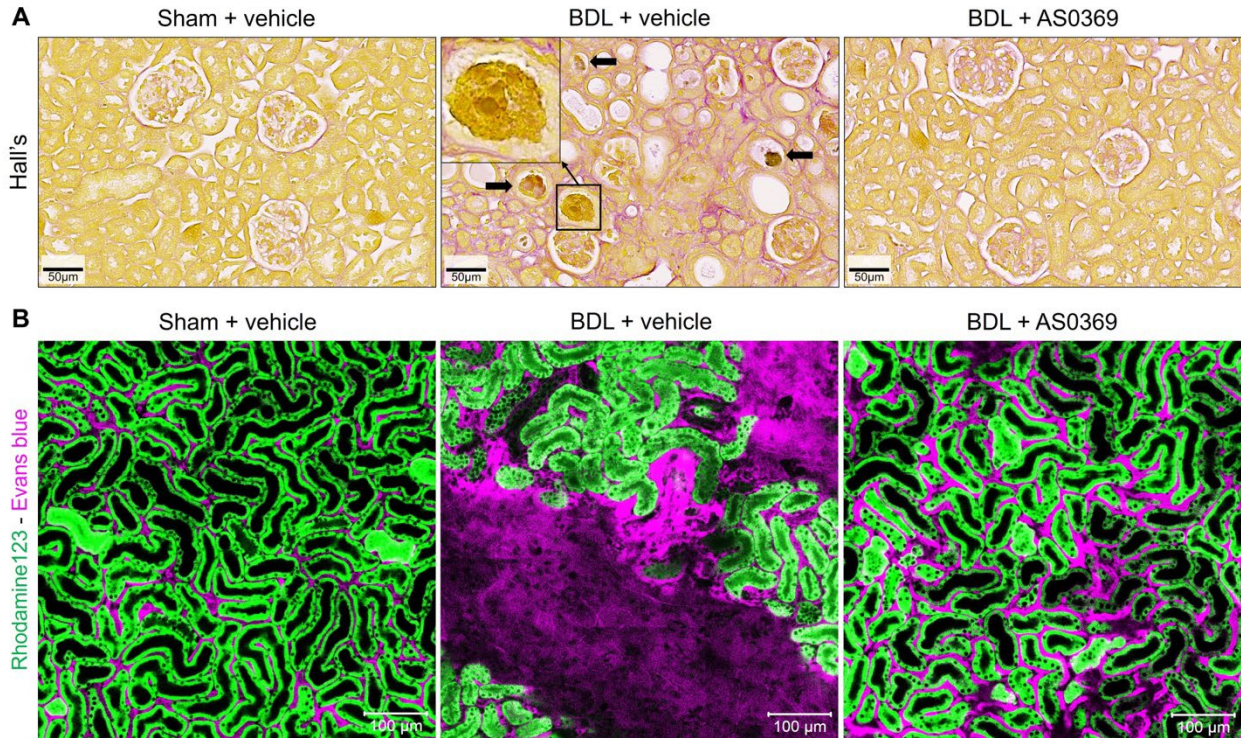
Fig. S13: ASBT inhibition prevents formation of Hall's positive bile casts and the leakiness of peritubular capillaries. A. Bile casts (arrows) visualized by Hall's stain; scale bars: 50 µm. **B.** Intravital imaging after tail vein injection of Evans blue (overviews); scale bars: 100 µm. The images correspond to the three treatment groups illustrated in Fig 5A of the main manuscript.
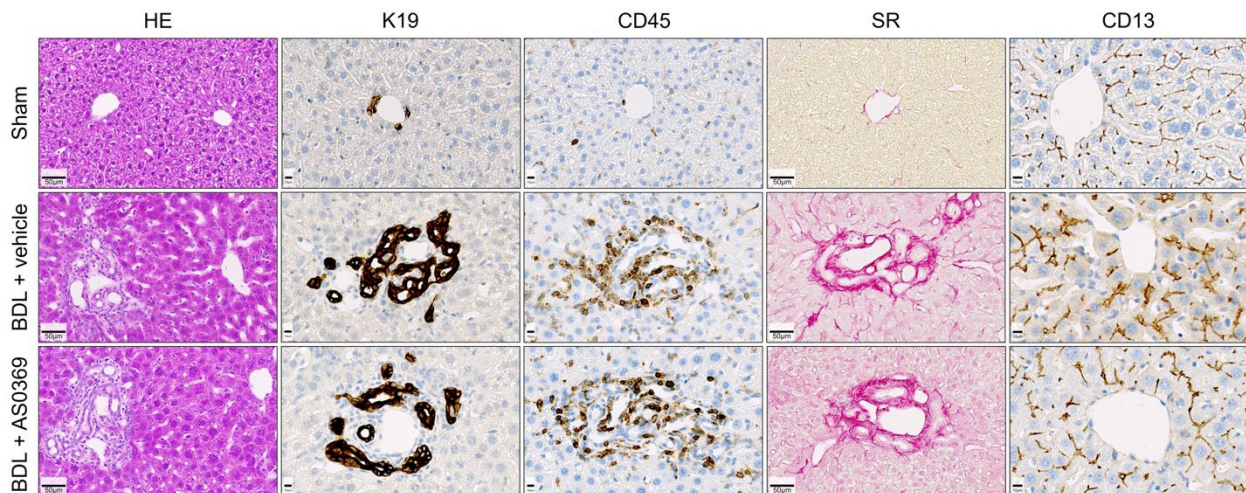
Fig. S14: Influence of ASBT inhibition on the liver. Histopathology (H&E and Sirius red), ductular reaction (K-19), leukocyte infiltration (CD45), and bile canaliculi (CD13) stainings; scale bars: 50 µm. The mice correspond to the three treatment groups illustrated in Fig 5A of the main manuscript.
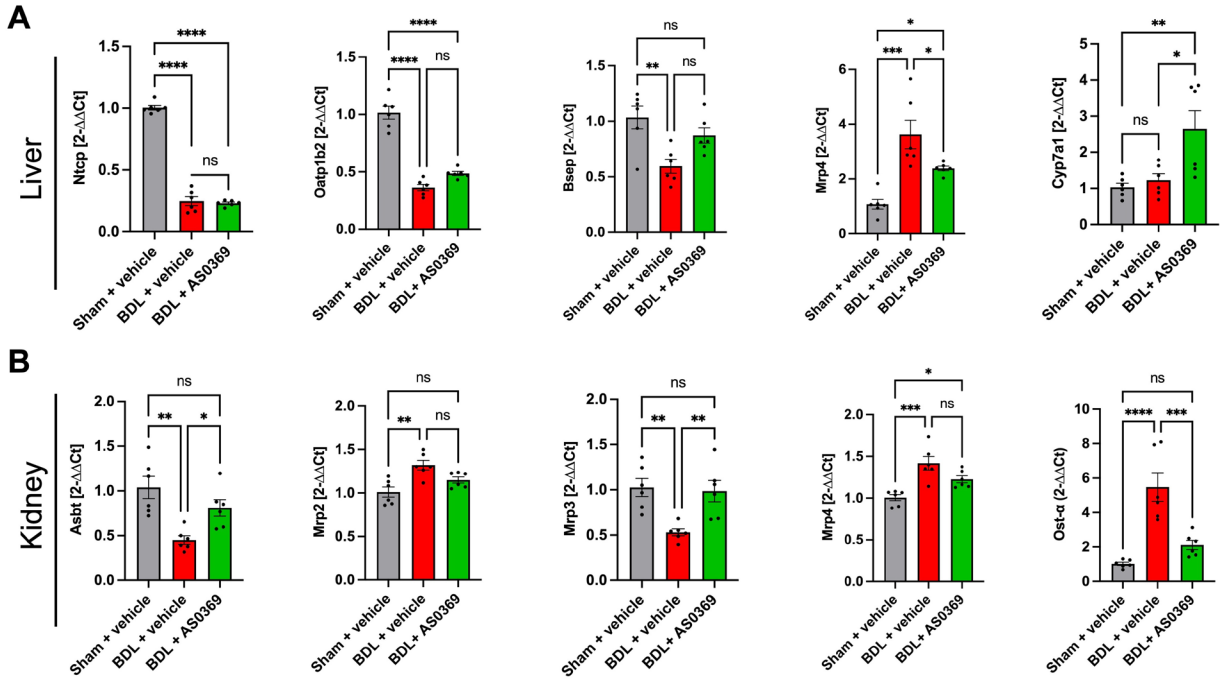
Fig. S15: RNA levels of bile acid carriers in liver and kidney tissue, and of *Cyp7a1* in the liver. The mice correspond to the three treatment groups illustrated in Fig 5A of the main manuscript. *p< 0.05; **p< 0.01; ***p< 0.001, ***p< 0.0001 compared to the sham controls, Dunn's multiple comparisons test.
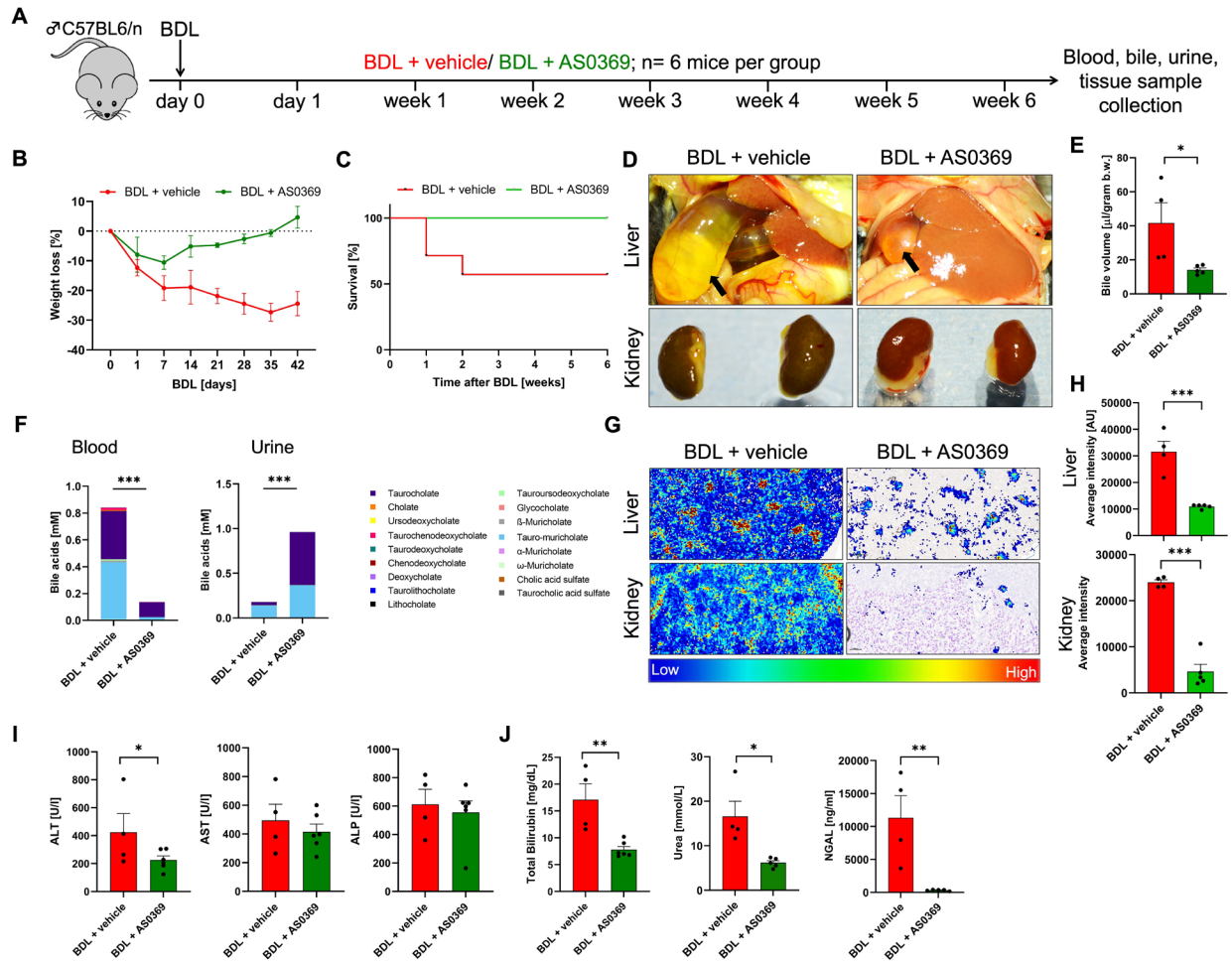
Fig. S16: Inhibition of ASBT prevents cholemic nephropathy in male mice after BDL. A. Experimental schedule. **B.** Bodyweight loss. **C.** Survival analysis. **D.** Gross pathology of the livers and kidneys. **E.** Gallbladder bile volume. **F.** Bile acid concentrations in blood and urine. **G, H.** MALDI-MSI of TCA in liver and kidney and corresponding quantifications. **I. J.** Clinical chemistry. *p< 0.05; **p< 0.01; ***p< 0.001 compared to the sham controls, Dunn's multiple comparisons test.

27
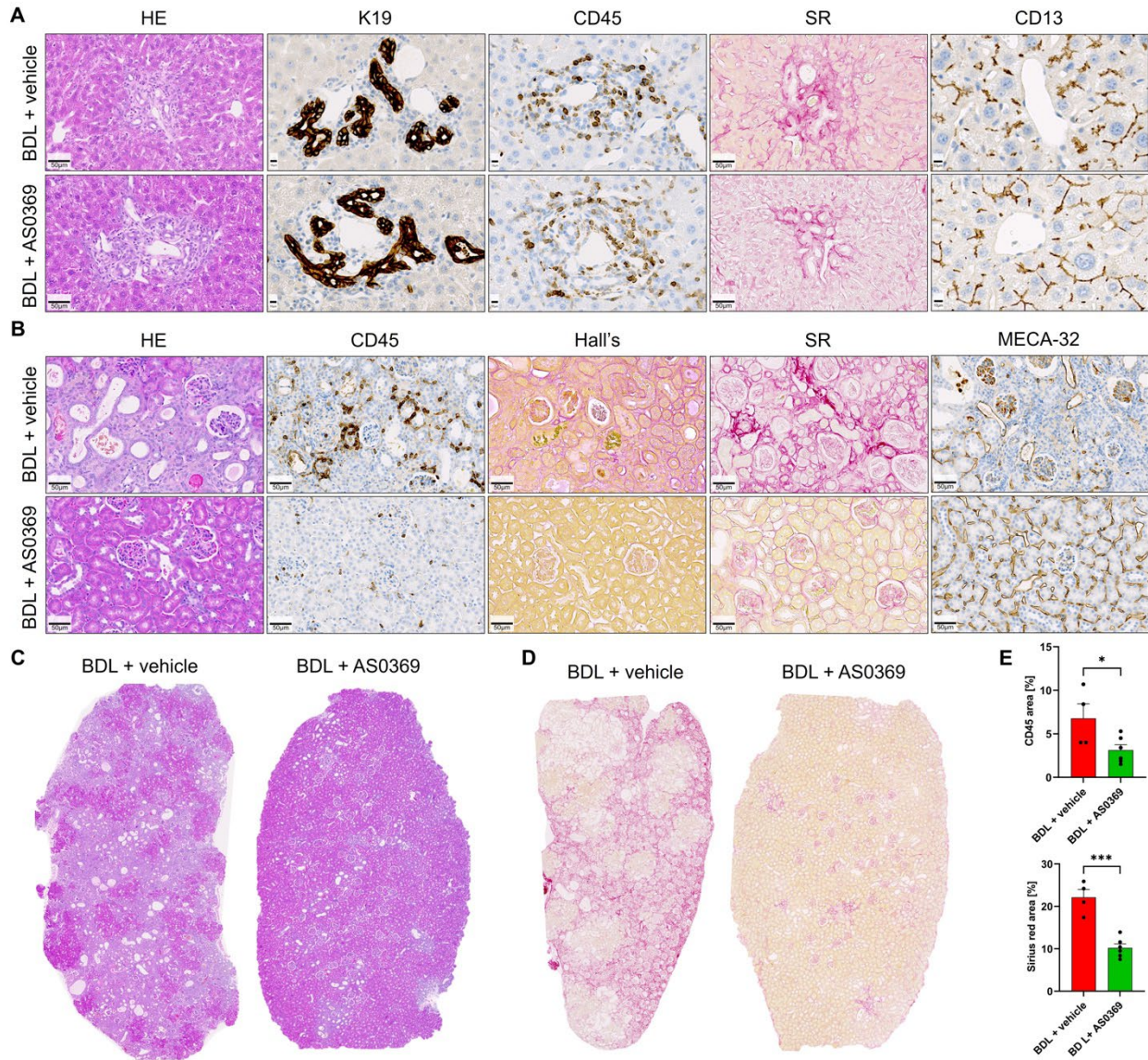
Fig. S17: Influence of ASBT inhibition on hepatic and renal histology. The treatment groups of the mice are illustrated in Suppl. Fig 17A. **A.** Liver histopathology. **B.** Kidney histopathology. **C-D.** Whole organ sections of the kidneys. **E.** Quantifications of CD45 and Sirius red signals in kidney tissue.
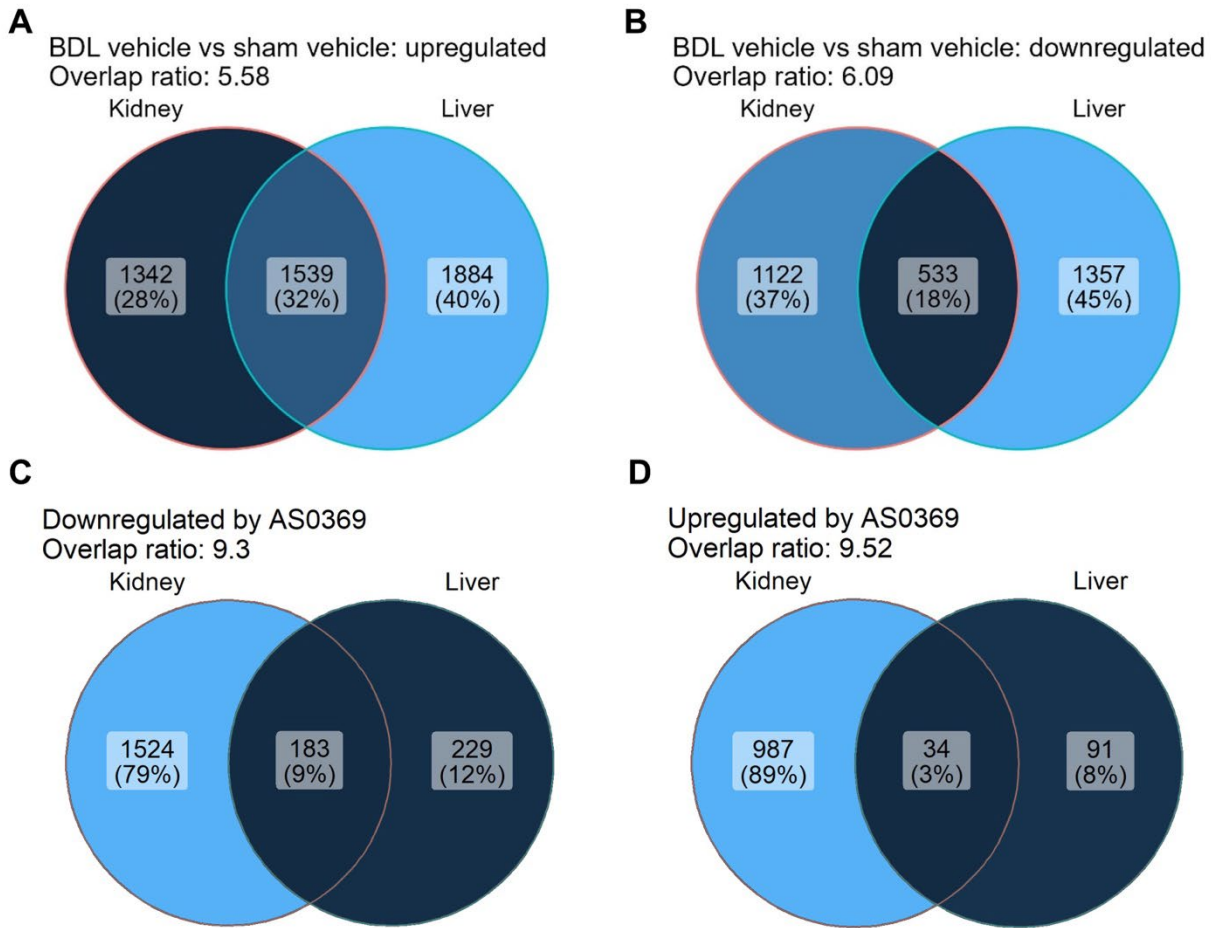
Fig. S18: Overlap analysis of differential genes in the kidney and liver. A. Overlap of up and downregulated genes due to BDL in kidney and liver. **B.** Overlap of the ASBT inhibitor (AS0369) response in the liver and kidney. The gene sets correspond to group 1a (left) and group 1b (right) of the DiPa plots shown in Fig 7C and 7I of the main manuscript. The overlap ratio indicates by which factor the number of genes in the overlap of both sets exceeds a randomly expected result.

Supplementary tables

Table S1A. Renal biopsies with and without cholemic nephropathy

Erlangen cohort				
n	Sex	Age (years)	Disease	Serum creatinine (mg/dL)
1	Male	49	Zero-time nephropathy	0.44
2	Female	61		0.62
3	Male	16		0.59
4	Female	57		0.78
5	Male	43		1.05
6	Male	24		0.98
7	Male	39		0.8
8	Male	63	Bile cast nephropathy	9
9	Male	75		7.9
10	Male	62		3.7
11	Male	62		3.8
12	Male	23		0.65
13	Male	52		3.53
14	Male	33		N.A.
Hannover cohort				
n	Sex	Age (years)	Disease	Serum creatinine (mg/dL)
1	Female	62	Zero-time nephropathy	N.A.
2	Female	64		N.A.
3	Female	68		N.A.
4	Female	56		N.A.
5	Male	54	Minimal Change	N.A.
6	Male	56		N.A.
7	Male	11		N.A.
8	Male	18		N.A.
9	Male	47		N.A.
10	Male	59	Cholemic Nephropathy	N.A.
11	Male	61		N.A.
12	Female	51		N.A.
13	Male	73		N.A.
14	Male	52		N.A.
15	Male	10		N.A.
16	Male	33		N.A.
17	Male	50		N.A.
18	Male	65		N.A.

Table S1B. Characteristics of patients with liver diseases and healthy volunteers

	Patients (n=67) with liver disease and total bilirubin >6 mg/dL			Healthy volunteers (n=36) without known liver and kidney disease			P-value[1]
	Median	25%-Percentile	75%-Percentile	Median	25%-Percentile	75%-Percentile	
Age (years)	49.5	39.0	58.3	41.5	31.0	57.8	ns
Total bilirubin (mg/dL)	15.9	7.7	22.2	0.80	0.70	1.00	<0.001
Sum bile acids (µmol/L)	151.2	63.0	266.9	3.25	1.80	5.33	<0.001
KIM-1 (pg/mL)	805.1	582.1	1608.8	48.5	29.3	75.8	<0.001
NGAL (ng/mL)	102.5	55.6	199.9	65.5	51.3	83.0	0.009
Cystatin C (ng/mL)	1148.5	782.1	1643.0	806.5	700.5	958.0	<0.001
Creatinine (mg/L)	790	600	1010	850	800	1000	ns
AST (U/L)	98.0	69.0	171.0	22.0	20.0	26.0	<0.001
ALT (U/L)	56.0	42.0	115.0	17.5	14.0	21.0	<0.001
ALP (U/L)	160.0	103.0	248.0	60.5	54.0	69.0	<0.001
GGT (U/L)	133.0	56.0	286.0	15.5	12.0	24.5	<0.001
CRP (mg/dL)	1.86	0.48	3.42	nt	nt	nt	
Sex	Male: n=41 (61.2%); Female: n=26 (38.8%)			Male: n=13 (36.1%); Female: n=23 (63.9%)			
UDCA therapy	Yes: n=21 (31.3%); No: n=46 (68.7%)			no			
Mean arterial pressure (mmHg)	<65: n=2 (3.0%); ≥65: n=65 (97.0%)			nt			
Condition	• Alcoholic liver disease: n=30 (44.8%) • Acute liver injury: n=8 (11.9%) • Cholestatic liver disease: n=7 (10.4%) • Post-transplant: n=7 (10.4%) • Alcoholic liver disease plus viral: n=2 (3.0%) • NASH: n=3 (4.5%) • Hepatic malignancy: n=2 (3.0%) • Other: n=8 (12.0%)			none			

[1]P-value of the Wilcoxon test for independent variables, two-sided test, comparing patients and healthy volunteers.
ns: not significant; nt: not tested.

Table S2: List of bile acids and internal standards with MRM transitions and MS parameters for quantification by LC-MS-MS.

Analyte	Internal Standard	Precursor Ion	Product Ion	CE (V)
ω-Muricholate (ωMCA)	d5-ωMCA	407.3	407.3	0
α-Muricholate (αMCA)	d5-αMCA	407.3	407.3	0
ß-Muricholate (ßMCA)	d5-βMCA	407.3	407.3	0
Tauro-α/ß-muricholate (TαßMCA)	d4-TßMCA	514.3	80.1	74
Tauro-ω-muricholate (TωMCA)	d4-TßMCA	514.3	80.1	74
7-Dehydrocholate (7-DHCA)	d4-TßMCA	405.3	405.3	38
Hyodesoxycholate (HDCA)	d4-UDCA	391.3	391.3	0
Cholate (CA)	d4-CA	407.3	343.4	36
Glycocholate (GCA)	d4-GCA	464.3	74.0	40
Taurocholate (TCA)	d4-TCA	514.3	80.1	74
Chenodeoxycholate (CDCA)	d4-CDCA	391.3	391.3	0
Taurochenodeoxycholate (TCDCA)	d4-TCDCA	498.3	80	80
Deoxycholate (DCA)	d4-DCA	391.3	345.3	32
Taurodeoxycholate (TDCA)	d4-TDCA	498.3	80.1	78
Ursodeoxycholate (UDCA)	d4-UDCA	391.3	391.3	0
Tauroursodeoxycholate (TUDCA)	d4-TUDCA	498.3	80.0	74
Lithocholate (LCA)	d5-LCA	375.3	375.3	0
Taurolithocholate (TLCA)	d4-TLCA	482.3	80.1	78
Cholic acid sulfate (CA-S)	d4-CA-S	487.2	96.9	58
Taurocholic acid sulfate (TCA-S)	d4-TCA-S	594.2	514.3	32
Internal Standard				
d5-ω-Muricholate (d5-ωMCA)		413.3	413.3	0
d5-α-Muricholate (d5-αMCA)		413.3	413.3	0
d5-ß-Muricholate (d5-ßMCA)		413.3	413.3	0
d4-Tauro-ß-muricholate (d4-TMCA)		518.3	80.1	74
d4-Cholate (d4-CA)		411.3	347.2	40
d4-Glycocholate (d4-GCA)		468.3	74.0	40
d4-Taurocholate (d4-TCA)		518.3	80.1	74
d4-Chenodeoxycholate (d4-CDCA)		395.3	395.3	0
d4-Taurochenodeoxycholate (d4-TCDCA)		502.3	80.0	86
d4-Deoxycholate (d4-DCA)		395.3	395.3	38
d4-Taurodeoxycholate (d4-TDCA)		502.3	80.0	82
d4-Ursodeoxycholate (d4-UDCA)		395.3	395.3	0
d4-Tauroursodeoxycholate (d4-TUDCA)		502.3	80.0	74
d5-Lithocholate (d5-LCA)		380.3	380.3	0
d4-Taurolithocholate (d4-TLCA)		486.3	80.1	90
d4-Cholic acid sulfate (d4-CA-S)		491.3	98.0	58
d4-Taurocholic acid sulfate (d4-TCA-S)		598.3	518.3	32

Table S3. Antibodies used for immunohistochemistry.

Target	Primary antibodies		Secondary antibodies	
	Antibody	Dilution	Antibody	Dilution
Cholangiocyte	Anti-cytokeratin 19 antibody, rabbit	1:500	Ultra-Map anti rabbit HRP	Automatic Discovery Ready to use
Bile canaliculi	Recombinant anti-CD13 antibody, rabbit	1:16000	Ultra-Map anti rabbit HRP	
Leukocytes	Anti-CD45 antibody, rat	1:400	Omni-Map anti rat HRP	
Endothelial cells	Anti-MECA-32 antibody, rat	1:250	Ultra-Map anti rat HRP	
ASBT	Anti-ASBT antibody, goat	1:500	Ultra-Map anti goat HRP	
ASBT	Anti-ASBT antibody, rabbit	1:50	Ultra-Map anti rabbit HRP	
AQP1	Anti-AQP1 antibody, rabbit	1:10000	Ultra-Map anti rabbit HRP	
TSC	Anti-TSC antibody, rabbit	1:2000	Ultra-Map anti rabbit HRP	

Table S4. Fluorescent markers and functional dyes used in the study.

Fluorescent marker	Marker for	Dose [mg/kg]	Vehicle	Two-photon excitation range [nm]
Hoechst 33258	Nuclei	5	PBS	700-800
TMRE	mitochondrial membrane potential	0.96	Methanol: PBS (1:1)	740-820
Cholyl-lysyl-fluorescein	Bile acid analogue	1	PBS	740-820
2',7'Dichlorofluorescein diacetate	Oxidative stress	0.5	DMSO	900-950
SYTOX green	Cell death	1.2	DMSO: PBS (1:100)	900-950
Fluorescein-coupled TCA	Bile acid analogue	1	PBS	740-820
Fluorescent marker	Marker for	Dose [mg/kg]	Vehicle	Confocal excitation range [nm]
Anti-CD31	Endothelial cells	0.08	PBS	381 - 459
Evans blue	Capillary leakiness	0.5	PBS	646 - 709
Rhodamine123	Mitochondrial membrane potential	0.8	Methanol: PBS (1:1)	498 - 532

Table S5. TaqMan gene assays.

Gene	TaqMan Assay ID
Abcb11	Mm00445168_m1
Abcc2	Mm00496899_m1
Abcc3	Mm00551550_m1
Abcc4	Mm01226381_m1
Cyp7a1	Mm00484150_m1
Egr1	Mm00656724_m1
GAPDH	Mm99999915_g1
Slc1a2	Mm01275814_m1
Slc10a1	Mm00441421_m1
Slc10a2	Mm00488258_m1
Slco1b2	Mm00451510_m1
Slc51a	Mm00521530_m1

Supplementary references

[1]   Ghallab A, Hofmann U, Sezgin S, Vartak N, Hassan R, Zaza A, et al. Bile Microinfarcts in Cholestasis Are Initiated by Rupture of the Apical Hepatocyte Membrane and Cause Shunting of Bile to Sinusoidal Blood. Hepatology 2019;69:666-683.

[2]   Tag CG, Sauer-Lehnen S, Weiskirchen S, Borkham-Kamphorst E, Tolba RH, Tacke F, et al. Bile duct ligation in mice: induction of inflammatory liver injury and fibrosis by obstructive cholestasis. J Vis Exp 2015.

[3]   Ghallab A, Celliere G, Henkel SG, Driesch D, Hoehme S, Hofmann U, et al. Model-guided identification of a therapeutic strategy to reduce hyperammonemia in liver diseases. J Hepatol 2016;64:860-871.

[4]   Gianmoena K, Gasparoni N, Jashari A, Gabrys P, Grgas K, Ghallab A, et al. Epigenomic and transcriptional profiling identifies impaired glyoxylate detoxification in NAFLD as a risk factor for hyperoxaluria. Cell Rep 2021;36:109526.

[5]   Reis LO, Sopena JM, Fávaro WJ, Martin MC, Simão AF, Reis RB, et al. Anatomical features of the urethra and urinary bladder catheterization in female mice and rats. An essential translational tool. Acta Cir Bras 2011;26 Suppl 2:106-110.

[6]   Leuthold P, Schaeffeler E, Winter S, Büttner F, Hofmann U, Mürdter TE, et al. Comprehensive Metabolomic and Lipidomic Profiling of Human Kidney Tissue: A Platform Comparison. J Proteome Res 2017;16:933-944.

[7]   Holland CH, Ramirez Flores RO, Myllys M, Hassan R, Edlund K, Hofmann U, et al. Transcriptomic Cross-Species Analysis of Chronic Liver Disease Reveals Consistent Regulation Between Humans and Mice. Hepatol Commun 2022;6:161-177.

[8]   Hall MJ. A staining reaction for bilirubin in sections of tissue. Am J Clin Pathol 1960;34:313-316.

[9]   Ghallab A, Hassan R, Hofmann U, Friebel A, Hobloss Z, Brackhagen L, et al. Interruption of bile acid uptake by hepatocytes after acetaminophen overdose ameliorates hepatotoxicity. J Hepatol 2022;77:71-83.

[10]   Hassan R, Gonzalez D, Hobloss Z, Brackhagen L, Myllys M, Friebel A, et al. Inhibition of cytochrome P450 enhances the nephro- and hepatotoxicity of ochratoxin A. Arch Toxicol 2022;96:3349-3361.

[11]   Zuiderveld K. Contrast Limited Adaptive Histogram Equalization. In: Paul S Heckbert (Hg): Graphics gems [IBM-ausg], 5 [Dr] Boston: Academic Press (The graphic gems series), S 474–485 2000.

[12]   Friebel A, Johann T, Drasdo D, Hoehme S. Guided interactive image segmentation using machine learning and color-based image set clustering. Bioinformatics 2022;38:4622-4628.

[13]   Breiman L. Machine Mearning 2001;45:5.

[14]   Bankhead P, Loughrey MB, Fernández JA, Dombrowski Y, McArt DG, Dunne PD, et al. QuPath: Open source software for digital pathology image analysis. Sci Rep 2017;7:16878.

[15]   Durix B, Chambon S, Leonard K, Mari J-L, Morin G. The Propagated Skeleton: A Robust Detail-Preserving Approach. In: Couprie M, Cousty J, Kenmochi Y, Mustafa N, editors. Discrete Geometry for Computer Imagery; 2019 2019//; Cham: Springer International Publishing; 2019. p. 343-354.

[16] Ghallab A, Hassan R, Myllys M, Albrecht W, Friebel A, Hoehme S, et al. Subcellular spatio-temporal intravital kinetics of aflatoxin B(1) and ochratoxin A in liver and kidney. Arch Toxicol 2021;95:2163-2177.

[17] **Reif R, Ghallab A**, Beattie L, Gunther G, Kuepfer L, Kaye PM, et al. In vivo imaging of systemic transport and elimination of xenobiotics and endogenous molecules in mice. Arch Toxicol 2017;91:1335-1352.

[18] Vartak N, Guenther G, Joly F, Damle-Vartak A, Wibbelt G, Fickel J, et al. Intravital Dynamic and Correlative Imaging of Mouse Livers Reveals Diffusion-Dominated Canalicular and Flow-Augmented Ductular Bile Flux. Hepatology 2021;73:1531-1550.

[19] Bábíčková J, Klinkhammer BM, Buhl EM, Djudjaj S, Hoss M, Heymann F, et al. Regardless of etiology, progressive renal disease causes ultrastructural and functional alterations of peritubular capillaries. Kidney Int 2017;91:70-85.

[20] Thévenaz P, Ruttimann UE, Unser M. A pyramid approach to subpixel registration based on intensity. IEEE Trans Image Process 1998;7:27-41.

[21] Ghallab A, Myllys M, Friebel A, Duda J, Edlund K, Halilbasic E, et al. Spatio-Temporal Multiscale Analysis of Western Diet-Fed Mice Reveals a Translationally Relevant Sequence of Events during NAFLD Progression. Cells 2021;10.

[22] Patro R, Duggal G, Love MI, Irizarry RA, Kingsford C. Salmon provides fast and bias-aware quantification of transcript expression. Nature Methods 2017;14:417-419.

[23] Team RC. R: A language and environment for statistical computing. R Foundation for Statistical Computing, Vienna, Austria https://wwwR-projectorg/ 2022.

[24] Love MI, Soneson C, Hickey PF, Johnson LK, Pierce NT, Shepherd L, et al. Tximeta: Reference sequence checksums for provenance identification in RNA-seq. PLoS Comput Biol 2020;16:e1007664.

[25] Love MI, Huber W, Anders S. Moderated estimation of fold change and dispersion for RNA-seq data with DESeq2. Genome Biology 2014;15:550.

[26] Zhu A, Ibrahim JG, Love MI. Heavy-tailed prior distributions for sequence count data: removing the noise and preserving large differences. Bioinformatics 2019;35:2084-2092.

[27] **Nell P, Kattler K, Feuerborn D**, Hellwig B, Rieck A, Salhab A, et al. Identification of an FXR-modulated liver-intestine hybrid state in iPSC-derived hepatocyte-like cells. J Hepatol 2022;77:1386-1398.

[28] Alexa A, Rahnenführer J, Lengauer T. Improved scoring of functional groups from gene expression data by decorrelating GO graph structure. Bioinformatics 2006;22:1600-1607.

[29] **Shinde V, Hoelting L**, Srinivasan SP, Meisig J, Meganathan K, Jagtap S, et al. Definition of transcriptome-based indices for quantitative characterization of chemically disturbed stem cell development: introduction of the STOP-Tox(ukn) and STOP-Tox(ukk) tests. Arch Toxicol 2017;91:839-864.

Author names in bold designate shared co-first authorship.